Zinc Oxide Transparent Thin Films For Optoelectronics

by

Karthik Sivaramakrishnan

A Dissertation Presented in Partial Fulfillment
of the Requirements for the Degree
Doctor of Philosophy

Approved November 2011 by the
Graduate Supervisory Committee:

Terry L Alford, Chair
Dieter K Schroder
Nathan Newman
David Theodore

ARIZONA STATE UNIVERSITY

December 2010

ABSTRACT

The object of this body of work is to study the properties and suitability of zinc oxide thin films with a view to engineering them for optoelectronics applications, making them a cheap and effective alternative to indium tin oxide (ITO), the most used transparent conducting oxides in the industry.

Initially, a study was undertaken to examine the behavior of silver contacts to ZnO and ITO during thermal processing, a step frequently used in materials processing in optoelectronics. The second study involved an attempt to improve the conductivity of ZnO films by inserting a thin copper layer between two ZnO layers. The Hall resistivity of the films was as low as 6.9×10^{-5} Ω-cm with a carrier concentration of 1.2×10^{22} cm^{-3} at the optimum copper layer thickness. The physics of conduction in the films has been examined. In order to improve the average visible transmittance, we replaced the copper layer with gold. The films were then found to undergo a seven orders of magnitude drop in effective resistivity from 200 Ω-cm to 5.2×10^{-5} Ω-cm The films have an average transmittance between 75% and 85% depending upon the gold thickness, and a peak transmittance of up to 93%. The best Haacke figure of merit was 15.1×10^{-3} Ω^{-1}.

Finally, to test the multilayer transparent electrodes on a device, ZnO/Au/ZnO (ZAZ) electrodes were evaluated as transparent electrodes

for organic light-emitting devices (OLEDs). The electrodes exhibited substantially enhanced conductivity (about 8×10^{-5} Ω-cm) over conventional indium tin oxide (ITO) electrodes (about 3.2×10^{-5} Ω-cm). OLEDs fabricated with the ZAZ electrodes showed reduced leakage compared to control OLEDs on ITO and reduced ohmic losses at high current densities. At a luminance of 25000 cd/m^2, the lum/W efficiency of the ZAZ electrode based device improved by 5% compared to the device on ITO. A normalized intensity graph of the colour output from the green OLEDs shows that ZAZ electrodes allow for a broader spectral output in the green wavelength region of peak photopic sensitivity compared to ITO. The results have implications for electrode choice in display technology.

Dedicated to my family Dr. S Sivaramakrishnan, Valsala Sivaramakrishnan, and Sriram Sivaramakrishnan, for their eternal love and companionship

ACKNOWLEDGMENTS

I consider it my privilege to acknowledge the help, assistance and support of the many individuals without whom this dissertation would not have been possible.

It is my honour to thank my research advisor Dr. T. L. Alford for his constant guidance, and invaluable suggestions during the past four years.

It gives me pleasure to thank the members of my dissertation committee including Dr. D. K. Schroder, Dr. D. Theodore, and Dr. N. Newman for taking the time to review my work and provide constructive feedback.

I am indebted to Tim Karcher for allowing my experiments and modifications with the magnetron sputter system. I would like to thank former colleagues Dr. Han, Dr. Zoo, and Dr. Thompson, for providing training on the operation of lab instruments. I would also like to thank Barry Wilkens, David Wright, Diana Convey, and Kenneth Mossman of the CSSS staff for training and assistance with instrument usage.

I would like to acknowledge the friendship and assistance of my lab mates Anil Indluru and Mandar Gadre.

Finally, the acknowledgements would be incomplete without thanking my father Dr. S Sivaramakrishnan, my mother Valsala Sivaramakrishnan, and my brother Sriram Sivaramakrishnan, without whose eternal love and companionship this research expedition would

have been impossible. At the same time, I would like to express my deep gratitude to dear friends, some oceans apart, who have always been there to share my joys and sorrows along the way.

TABLE OF CONTENTS

Page

LIST OF TABLES xii

LIST OF FIGURES xiii

CHAPTER

1 INTRODUCTION 1

1.1. TRANSPARENT CONDUCTING OXIDES 1

1.2. SOLAR CELLS 7

1.3. OLEDs AND FLAT-PANEL DISPLAYS 10

1.4. LOW-EMISSIVITY COATINGS 11

1.5. SILVER CONTACTS AND LOW-EMISSIVITY COATINGS 12

1.6. SUMMARY 13

2 EFFECT OF THERMAL PROCESSING ON SILVER THIN FILMS OF VARYING THICKNESS DEPOSITED ON ZINC OXIDE AND INDIUM TIN OXIDE 15

2.1. INTRODUCTION 15

2.2. EXPERIMENTAL 16

2.3. RESULTS 18

2.4. DISCUSSION 28

2.5. CONCLUSION 37

CHAPTER Page

3 THE ROLE OF COPPER IN ZnO/Cu/ZnO THIN FILMS FOR FLEXIBLE ELECTRONICS 38

3.1. INTRODUCTION 38

3.2. EXPERIMENTAL 40

3.3. RESULTS 44

3.4. DISCUSSION 58

3.5. CONCLUSION 67

4 ZnO/Au/ZnO HIGH CONDUCTIVITY TRANSPARENT CONDUCTING OXIDES ON POLYETHYLENE NAPHTHALATE 68

4.1. INTRODUCTION 68

4.2. EXPERIMENTAL 70

4.3. RESULTS 72

4.4. DISCUSSION 79

4.5. CONCLUSION 88

5 ZnO BASED TRANSPARENT ANODES FOR OLEDs 90

5.1. INTRODUCTION 90

5.2. EXPERIMENTAL 92

5.3. RESULTS AND DISCUSSION 93

5.4. CONCLUSION 98

6 CONCLUSIONS

Page

6.1. SUMMARY OF RESEARCH 101

3.2. FUTURE WORK 106

REFERENCES 107

APPENDIX

A LIST OF PUBLICATIONS 120

LIST OF TABLES

Table Page

Table 1.1. *N*-type dopants used and the optimized concentrations to give minimum resistivities, along with the obtained carrier concentrations …… 8

Table 2.1. [111] peak parameters from [111] pole figure texture analysis on Ag/ITO and Ag/ZnO samples…… 25

Table 3.1. Haacke figure of merit for the multilayer films with differentcopper thicknesses 61

Table 4.1. Sheet resistance in Ω/sq. as a function of annealing time for a thin (3 nm) and thick (12 nm) Au film in the ZnO/Au/ZnO structures 80

Table 4.2. Sheet resistance in Ω/sq. under different static bend conditions on a tube of 2” diameter for a thin and thick Au film in the ZnO/Au/ZnO structures 81

Table 4.3. Haacke figure of merit for the multilayer films with different gold thicknesses 89

LIST OF FIGURES

Figure Page

FIG. 1.1. A plot of percentage transmission (*T*) and reflection (*R*) at different energies 3

FIG. 1.2. Layers of a solar cell 9

FIG. 2.1. Electrical resistivity of Ag of various thicknesses on: (a) ITO and, (b) ZnO as a function of annealing temperature 20

FIG. 2.2. 2.0 MeV RBS spectra for: (a) 25 nm, (b) 45 nm, and (c) 60 nm Ag films on ITO.. 21

FIG. 2.3. 2.0 MeV RBS spectra for: (a) 25 nm, (b) 45 nm, and (c) 60 nm Ag films on ITO.. 22

FIG. 2.4. (111) pole figure profiles for 45 nm film of Ag on: (a) ITO and (b) ZnO as deposited, and annealed at 400 °C and 600 °C for 1 h in vacuum 23

FIG. 2.5. (200) pole figure profiles for 45 nm film of Ag on: a) ITO and b) ZnO as deposited, and annealed at 400 °C and 600 °C for 1 h in vacuum .... ……………………………… 26

FIG. 2.6. 3D AFM image of 25 nm of Ag film on a) ITO and b) ZnO substrates 27

FIG. 2.7. A schematic illustration of self-assembled Ag-island formation and the consequent reduction of backscattered ion intensity 31

Figure Page

FIG. 2.8. Arrhenius plot of agglomeration of the 45 nm films of Ag on ITO and ZnO 36

FIG. 3.1. Glancing angle XRD profile showing the largely amorphous structure of ZnO in the ZnO/Cu/ZnO multilayers 45

FIG. 3.2. Resistivity of the ZnO/Cu/ZnO thin films as a function of copper layer thickness... 46

FIG. 3.3. Sheet resistance of the ZnO/Cu/ZnO thin films as a function of copper layer thickness... 48

FIG. 3.4. Carrier concentration of the ZnO/Cu/ZnO thins films as a function of copper layer thickness... 49

FIG. 3.5. Hall mobility of the ZnO/Cu/ZnO thins films as a function of copper layer thickness... 50

FIG. 3.6. Optical transmittance spectra relative to the PEN substrate for ZnO/Cu/ZnO thin films as a function of Cu thickness....... 51

FIG. 3.7. XPS profiles of the ZnO/Cu/ZnO samples showing atomic concentration of the various elements with sputter depth for (a) 3 nm, and (b) 8 nm Cu thickness structures 53

FIG. 3.8. Intensity of Cu LMM line with depth of sputter during XPS for (a) 3 nm, and (b) 8 nm thick Cu layer structures is also shown. The 3-D representation of (b) is shown in (c)........................ 54

FIG. 3.9. Pole figure profile of ZnO (002) texture showing intensity plotted against angle of tilt, ψ 55

Figure Page

FIG. 3.10. Cross-section TEM micrographs of ZnO/Cu/ZnO films with varying Cu thickness: (a) 3 nm, (b) 6 nm, and (c) 8 nm......... 57

FIG. 3.11. Plot of absorption coefficient versus energy of photons showing the Burstein-Moss effect in the ZnO/Cu/ZnO multilayer films with increasing copper thickness 63

FIG. 4.1. Effective resistivity of the ZnO thin films as a function of embedded gold layer thickness.. 73

FIG. 4.2. Sheet resistance of the ZnO thin films as a function of embedded gold layer thickness.. 74

FIG. 4.3. Carrier concentration of the ZnO thins films as a function of embedded gold layer thickness.. 76

FIG. 4.4. Hall mobility the ZnO thins films as a function of embedded gold layer thickness 77

FIG. 4.5. Transmission spectra (relative to the substrate) in the visible spectral range for ZnO thin films showing variation with thickness of the embedded gold layer.................................. 78

FIG. 4.6. Nomarski images of ZnO/Au(12nm)/ZnO (a) before and (b) after static bend testing 82

FIG. 4.7. Schematic showing the band diagram for small metal particles with significant separation between them................ 84

FIG. 5.1. Current density as a function of voltage for OLEDs using ITO and ZAZ multilayers as anodes...................................... 94

Figure Page

FIG. 5.2. A 5 μm × 5 μm AFM scan showing the surface morphology of the ZAZ anodes 95

FIG. 5.3. Luminance as a function of voltage for OLEDs using ITO and ZAZ multilayers as anodes.. 97

FIG. 5.4. Spectral output from the OLEDs with ITO and ZAZ as electrodes…... 100

CHAPTER 1

INTRODUCTION

1. 1. TRANSPARENT CONDUCTING OXIDES

Transparent conducting oxides (TCOs) comprise a class of materials that are unique in the sense that two seemingly conjugate properties co-exist [1]. TCOs find applications [2, 3] in flat-panel displays (*e.g.*, LCDs), solar cells, electromagnetic shielding of CRTs used for video display terminals [4], electrochromic windows, low-emissivity windows in buildings, defrosting windows, oven windows, static dissipation, touch-panel controls, and invisible security circuits. In materials, the property of conductivity is strongly coupled to a second property, namely, the lossy part of the refractive index or the extinction coefficient [1]. In this regard, materials like metals that are highly conductive will not normally transmit visible light, while highly transparent media like oxide glasses behave as insulators. The challenge for achieving materials that are both conducting and optically transmissive is to understand the fundamental materials structure/property relationships that drive these properties so that they may be decoupled such that the material retains transparency while becoming more electrically conductive. To an extent, many phenomenological approaches based upon well-understood physical principles have been reported to achieve materials having these properties. An overview of these approaches will be presented along with an idea to further the development of TCO technology.

In order to understand the progress made in this field it is essential to first introduce the physics involved in these semiconductors.

1.1.1. Transmission

The wide-bandgap semiconductors have a window of transmission as illustrated in Figure 1.1.

The region of optical transparency 'b' becomes bounded at the high-energy side by the strongly allowed electronic bandgap transition between the valence band maximum and the conduction band minimum and at the low energy side by the free carrier or plasma resonance absorption. The free carriers will interact with an applied optical field through the polarization. Consider a free carrier of mass m weakly bound in a lattice by a restoring force with a force constant k_f . If the applied field oscillates at a high frequency such that the free carrier mass inertia precludes motion, there will be no coupling to the field, no loss due to absorption, and the transmission will be high. However, if the weakly bound carrier can freely respond to the field, there will be loss.

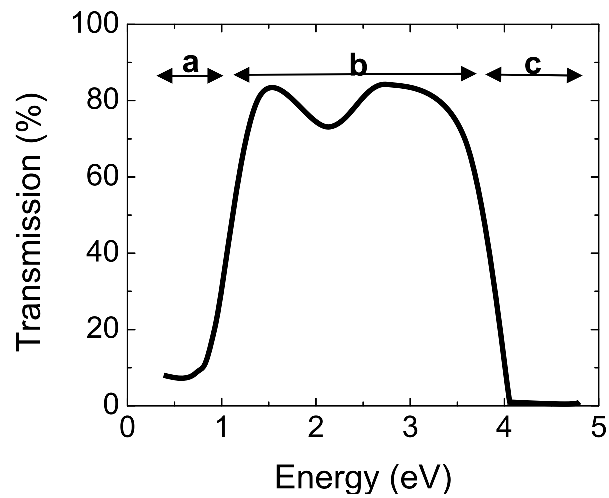

FIG. 1.1. A plot of percentage transmission (*T*) and reflection (*R*) at different energies [1]

1.1.2. Conduction and Scattering

Conduction is usually studied in terms of conductivity which is written as [5]:

$$\sigma = ne\mu \qquad (1.1)$$

where σ is the conductivity, n is the number of charge carriers, e is the charge on the carrier, and μ is the mobility. Equation 1 relates the conductivity to the number of charge carriers and their mobility. These then are taken as the important parameters to be used for characterization of charge transport in conducting materials. It is understood that the mobility generalizes all the forces acting on the electron in the conducting solid. Mobility can be stated as:

$$1/\mu = 1/\mu_i + 1/\mu_l + 1/\mu_g \qquad (1.2)$$

where μ_i represents ionized impurity scattering, μ_l accounts for lattice scattering, and μ_g for scattering at the grain boundaries. The effect and extent of these various scattering mechanisms must be taken into account to determine the conductivity in a material.

Recent studies push the envelope of earlier work through understanding at a fundamental level the microscopic nature of the conductivity process in order to discover the role of chemical structure, bonding, and film morphology on charge transport. For instance, stoichiometry [6] can determine the presence of native defects in the TCO. Native defects play a very crucial role [7] in the formation of defect energy

levels. Residual stress in the material can affect conduction by altering charge carrier mobility. Microstructure also can play a role through, for instance, scattering at the grain boundaries. The nature of the surface and interface can also play a significant role. This includes how interfacial chemical interactions between the film and the substrate affect properties.

For thin-film transparent electrodes, TCO semiconductors such as impurity-doped ZnO, In_2O_3, SnO_2, and multicomponent oxides composed of combinations of these binary compounds are the best candidates for practical use. Recently, the demand for indium tin oxide (ITO) thin-film transparent electrodes has dramatically increased in the field of optoelectronic devices. If the increase in usage of ITO films for flat panel displays and solar cells continues, not only will the price of ITO continue to rise but also the availability of indium may be jeopardized in the near future. The development of alternative TCO materials is necessary to resolve this serious problem. It should also be noted that for applications involving reducing atmospheres at high temperatures and hydrogen plasma, doped ZnO films are more stable than ITO films. As another specialized application, doped ZnO films can be advantageously used with thin-film solar cells, because ZnO films with a textured surface structure are more easily produced on relatively low temperature substrates than textured SnO_2 films [8]. On the practical side, the advantages with ZnO include the availability of large-area ZnO substrates [9] and high radiation resistance [10].

Good transparency and conductivity have been obtained in *n*-type ZnO as shown in Table 1.1 [11]. However, there is still scope for reducing the conductivity by about an order of magnitude. There has also been little success in making high conductivity *p*-type ZnO because of the asymmetric doping limitation. This is essential for applications which involve using homojunctions, like LEDs and laser diodes.

There are several advantages offered by dielectric-metal-dielectric electrodes over convention *n*-doped oxide electrodes. The electrical conductivity is significantly improved. Also, high conductivity is attained in the as-deposited condition, thus obviating the need for high temperature processing in order to improve conductivity. This makes the films suitable for deposition on low temperature polymer substrates. The addition of a ductile metal layer also provides improved robustness under mechanical strain. [12] The transparent oxide layer deposited on top of the metal layer provides a protective cover from the environment while simultaneously serving as an anti-reflection layer. The transparent oxide layer under the metal serves as a bonding layer to the substrate and a phase-matching layer. So while traditional transparent conductors provide reasonably high transmittance values but are limited in their conductivity, these transparent oxide-metal-oxide multilayers can simultaneously provide very high transparency and conductivity.

Known techniques can be used to deposit each of the layers in the

composite films. It has been found, however, that it is necessary to deposit these layers so that they are continuous and inter-diffusion is minimized. The exact method of deposition will depend upon parameters such as the various materials used for each of the layers, their thicknesses, the availability of equipment, *etc:* Some suitable techniques include RF and DC sputtering and reactive sputtering, thermal evaporation, electron beam evaporation, and chemical vapor deposition.

1. 2. SOLAR CELLS

Figure 2.2 shows the different layers including the typical location of the transparent conducting oxide layer. Bulk heterojunction organic solar cells (OSCs) have recently attracted considerable interest for use in the next generation of renewable energy sources due to their simple cell structure, simple process, low cost, and possibility of continuous roll-to-roll process in the atmosphere [13]. A key merit of OSCs is their potential for low cost and large area production based on continuous roll-to-roll coating. Therefore, it is necessary to develop low cost transparent anode materials, which can be prepared at the lowest possible temperature, to enable the low cost production of OSCs. However, most OSCs reported so far are usually fabricated on dc or rf sputtered polycrystalline indium tin oxide (ITO) electrodes prepared at a temperature above 300 °C. [13]

Table 1.I *N*-type dopants used and the optimized concentrations to give minimum resistivities, along with the obtained carrier concentrations [11]

Dopant	Dopant (Wt %)	Resistivity (10^{-4} Ω–cm)	Carrier concentration (10^{20} cm^{-3})
Al_2O_3	1-2	0.85	15.0
Ga_2O_3	2-7	1.2	14.5
B_2O_3	2	2.0	5.4
Sc_2O_3	2	3.1	6.7
SiO_2	6	4.8	8.8
V_2O_3	0.5	5.0	4.9
F	0.5 (at %)	4.0	5.0
None	0	4.5	2

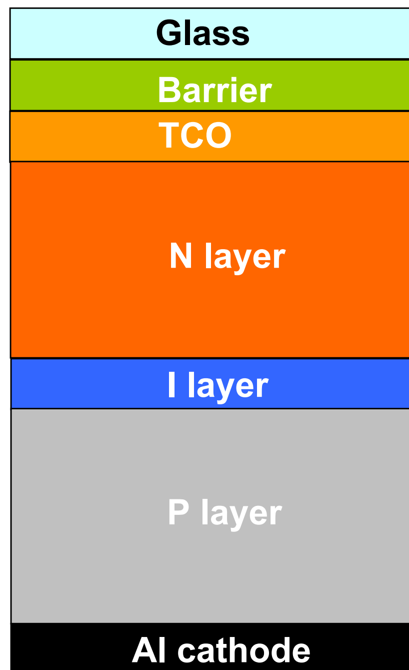

FIG. 2.2. Layers of a solar cell

Considering the cost advantages of OSCs, ITO electrodes are not suitable due to the high cost of indium (the main component of ITO) and its limited availability. For these reasons, indium-free transparent conducting oxides (TCOs), single-walled carbon nanotube films, and organic electrodes have been explored as potential low cost anode materials. [14] Recently, Ga-doped ZnO (GZO) electrodes have been employed as inexpensive anode materials for organic light-emitting diodes (OLEDs) and OSCs. [15] There is scope for exploring the use of ZnO-based dielectric-metal-dielectric films for high as-deposited conductivity indium-free electrodes.

1. 3. OLEDs AND FLAT-PANEL DISPLAYS

Organic light-emitting devices are ideal for flat panel display applications due to their full color gamut and thin form factor. Integration of dielectric-metal-dielectric electrodes with OLEDs has been demonstrated to provide significant improvements in the operational characteristics of these devices, especially for high current densities where ohmic losses become significant in the dielectric-only anodes. [12] The reduction in ohmic losses in the anode is especially advantageous for high-brightness and passive-matrix displays where higher momentary brightness is necessary. It has been shown by angle dependent electroluminescence (EL) spectra for OLEDs on ITO-Metal-ITO (IMI) electrodes and ITO anodes, that the maximum wavelength shift and the FWHM of the emission peak are lesser with the IMI anodes than with ITO. [12]

The resistance of the transparent row electrode directly limits the drivable screen size of flat panel displays. Transparent components having better performance are key components of the next generation of flat displays. Dielectric-metal-dielectric (DMD) structures show promise for use as a transparent conductor in flexible displays. They provide significantly reduced sheet resistance compared to ITO, and improved bending properties both as a function of radius and as a function of cycling.

1. 4. LOW-EMISSIVITY COATINGS

Highly transparent heat-reflective films (*i.e.,* films with high transmittance in the visible range and high reflectance in the infrared range) are produced for architectural glass for the purpose of saving energy for air conditioning. Moreover, these films are used as transparent electrically conductive films for automotive glass because of their low electrical resistance.

There are two types of transparent heat-reflective films: (1) single-layer films of highly degenerated semiconductors with a wide energy gap, *e.g.,* ITO, tin oxide, and cadmium tin oxide; (2) multilayer films consisting of oxide layers and thin metal layers, *e.g.,* TiO_2-Ag-TiO_2, SnO_2-Ag-SnO_2, and ITO-Ag-ITO; the metal layer reflects light in the infrared range and the oxide layer suppresses the reflection from a metal layer in the visible. Multilayer transparent heat-reflective films have higher reflectance in the far-infrared than single-layer semiconductor films. Multilayer films with a silver layer are

not stable both thermally and chemically because the optical and electrical properties of the silver layer are easily degraded by thermal oxidation and corrosion by chlorine and sulfur. [16] Thus, the usefulness of these films is limited. As a consequence, there is still a need for stable and durable heat-reflective films.

1. 5. SILVER CONTACTS AND LOW-EMISSIVITY COATINGS

Silver on ITO is used in low-emissivity and anti-solar coatings on glasses and polymers. [17] Their wide utilization for energy efficient windows in buildings and vehicles has led to considerable research on the physics of thin silver films. However, even minor improvements might lead to energy savings or even broader utilization, which is the main motivation to revisit the physics of thin silver films deposited on ITO and ZnO transparent substrates. Low emissivity, ε_n, is directly related to low sheet resistance, R_w. For low resistance (less than the impedance of vacuum, $R_w \ll Z_0 = 377\ \Omega$), and long wavelength of the electromagnetic waves ($\lambda > 3\ \mu m$), the simple relation $\varepsilon_n = 0.0106\ R_w$ holds for the emissivity in the direction normal to the surface [18]. Silver is known to grow in Volmer-Weber (island) mode on oxide substrates [19]. Incoming silver atoms are mobile on the surface at room temperature until they find an energetically preferred site. As more silver atoms are supplied to the surface, silver islands will grow and coalesce to form a contiguous but not-yet continuous film. This is the onset of conductivity. With further film growth, the remaining gaps between islands

are filled and a polycrystalline, well-conducting film is formed.

Silver, with its low resistivity, is an ideal contact material. Silver could serve as a contact to ITO on flexible stainless steel substrates, which allow for high temperature processing of flexible substrates. [20] However, ITO costs are increasing due to the scarcity of Indium. [21] ZnO is therefore being explored as a low cost alternative to ITO. It is therefore important to do a comparitive study of the behavior of Ag contacts on these two oxides. High conductivity requires tight control of the silver film properties such as grain size, preferred orientation, and contamination [22, 23].

1. 6. SUMMARY

The objective of this body of work is to study the properties and suitability of ZnO thin films with a view to engineering them for optoelectronics applications, making them a cheap and effective alternative to indium tin oxide, the most used transparent conducting oxides in the industry.

Initially, a study was undertaken to examine the behavior of silver contacts to ZnO and ITO during thermal processing, a step frequently used in materials processing in optoelectronics. It is found that the agglomeration of the silver films at higher temperatures can be delayed considerably by small increases in thicknesses of the deposited metal. Then an attempt has been made to improve the conductivity of ZnO films by inserting a thin copper layer between two ZnO layers. This is found to results in higher

conductivity than can be obtained by a traditional doping approach. The physics of conduction in the films has been examined. The transmittances were found to be lower than can be obtained by doping and reasons for transmission losses have been analysed. In order to improve the average visible transmittance, we replaced the copper films with gold films as thin gold films are known to be highly transparent, and the exact transparencies can vary depending on the quality of the deposited film, which could be determined by grain boundary energies of the metal, and surface and interface energies of the metal, oxide and metal-oxide interface. It can also be governed by the extent of phase-matching of light at the metal-oxide interface. Success in depositing high conductivity films without significant transmission losses could open up the possibility of better transparent electrodes for use in flat-panels, photovoltaics, and even LEDs. One of the big challenges in the area of ZnO research has been to obtain *p*-type majority carriers in the films. A review of the literature is documented and an idea is proposed for preparation of *p*-type ZnO films.

CHAPTER 2

EFFECT OF THERMAL PROCESSING ON SILVER THIN FILMS OF VARYING THICKNESS DEPOSITED ON ZINC OXIDE AND INDIUM TIN OXIDE

2. 1. INTRODUCTION

Transparent conducting oxides (TCOs) are a unique class of materials that exhibit simultaneous transparency and conductivity.[1] TCOs find applications[2,3] in the optoelectronics industry through use in flat-panel displays (*e.g.*, liquid crystal displays), solar cells, and electromagnetic shielding of CRTs used for video display terminals.[4] They are also used to make electrochromic windows, low-emissivity windows in buildings, defrosting windows, oven windows, static dissipation, touch-panel controls, and invisible security circuits. A good transparent conducting oxide must have high electrical conductivity and high transmittance in the desired wavelength region for the particular application.

Transparent conducting oxides such as doped ZnO, In_2O_3, and SnO_2 are the best candidates for thin-film transparent electrodes.[5] Presently, indium tin oxide (ITO) is commercially the most popular transparent conducting oxide in the optoelectronics industry because of its low resistivity (~$1x10^{-4}$ Ω-cm) and high optical transmittance (~ 85%)[6]; however, indium being a scarce resource makes ITO expensive. As a

consequence, there is a need for alternative commercially viable TCOs. ZnO when doped has the capability to show good electrical conduction and optical transmission in the visible region due to its high band gap of approximately 3.4 eV at room temperature. Besides, it also has practical advantages like the easy availability of large-area ZnO substrates[7] and good radiation resistance.[8]

Thin films of silver are used for applications such as low-emissivity coatings on tempered glass and on bent glass panes for vehicles. They could also be used as contacts for photovoltaic devices on flexible stainless steel substrates.[9] The sheet resistance of these films is greatly influenced by scattering of conduction electrons at defects, grain boundaries, and surfaces. Therefore, it is desirable to produce ultrathin films with large aligned grains and very smooth surfaces.[10] The silver layer could be subject to high temperatures in the processing stages for these applications[11]; this makes it essential to understand the annealing behavior of the silver. In this study, we deposit different thicknesses of Ag on ZnO and on ITO to study the changes in texturing and surface roughness of the Ag films after annealing at different temperatures. The work will elucidate the influence of thermal processing on the structural and electrical property changes in the Ag films.

2. 2. EXPERIMENTAL

Magnetron sputtering was used in the preparation of the samples.

The base pressure prior to deposition was approximately $1x10^{-7}$ Torr. Substrate to target distance was 6 cm and was maintained at the same value for all experiments. Thin films layers of ZnO and ITO were deposited on Si wafers by rf magnetron sputtering. Then without a vacuum break, Ag films of varying thicknesses were sputtered using dc magnetron sputtering at a pressure of 10 mTorr and 40 W power. The sputtering targets used in this experiment were 99.999% In_2O_3 containing 10 wt% SnO_2, 99.999% pure ZnO, and 99.99% Ag. The ZnO and ITO thicknesses were kept fixed at 20 nm and 40 nm, respectively. The Ag thickness was varied accordingly: 25 nm, 45 nm, and 60 nm. After deposition, the samples were annealed in a vacuum (base pressure ~ 10^{-8} Torr) for 1 hr at various temperatures (300, 400, 500, 600, and 650 ^{o}C) in order to investigate the changes in Ag film behavior. Resistivities of the Ag films were measured using an in-line, four-point probe configuration.

Rutherford backscattering spectrometry (RBS) was used for thickness determination of the as-deposited films. It was also used for studying changes brought about by annealing the Ag films. RBS analysis was performed in a vacuum of 10^{-6} Torr using a 2.0 MeV He^{++} ion beam and total accumulated charge of 20 μC in a General Ionex Tandetron accelerator. Sample and detector were in the Cornell geometry such that the backscatter detector is directly below the incident beam. The samples were tilted to 60° off normal incidence to increase the depth resolution. Energy spectra were

obtained using a surface-barrier detector and were analyzed using the RUMP computer simulation program.[12]

Surface morphology of the Ag films was studied using atomic force microscopy (AFM) in acoustic mode (tapping mode), using a Molecular Imaging Pico SPM system. The images were used to study the effect of annealing on film roughness and film surface morphology.

The phase of the as-deposited bilayer films was investigated by x-ray diffraction analysis (XRD) using a Philips X'pert multipurpose diffractometer system with Cu K_α radiation incident on the sample at a 1° glancing angle. The glancing angle configuration is used to limit x-ray penetration to the thin film mostly, thus reducing the occurrence of substrate peaks and background noise. Texture evolution of the Ag films was investigated by pole figure analyses. Texture along the (111) and (200) poles was measured with the sample tilt (ψ) varied from 0° to 85°.

2. 3. RESULTS

Resistivity changes in the Ag films on ITO and ZnO as a function of annealing temperature are shown in Fig. 2.1. For both Ag on ITO and Ag on ZnO, the thicker silver film results in a lower overall resistivity of the as-deposited samples. The resistivity decrease in the as-deposited samples however is lesser with increasing Ag film thickness. Among the annealed samples, the 25 nm film of Ag on ITO and ZnO is found to show a sudden increase in resistivity after annealing at 300 ^{o}C. The 45 nm films of Ag on

ITO and ZnO are stable up to 500 ^oC before showing a dramatic increase in resistivity. The 60 nm of Ag films on ITO and ZnO are completely stable even at 600 ^oC and began to show a significant increase in resistivity only at 650 ^oC.

The backscattering results shown in Fig. 2.2(a) for a 25 nm film of Ag on ITO shows a reduced intensity in channel number 290 to 320 upon annealing at 300 ^oC. The RBS spectrum in Fig. 2.3(a) for the 25 nm film of Ag on ZnO shows similar behavior. The 45 nm films of Ag on ITO and ZnO show a drop in intensity of the Ag peak at 600 ^oC as shown in the Fig. 2.2(b) and Fig. 2.3(b). The 60 nm films show reduced intensity only at 650 ^oC. It is also observed that as the temperature of anneal increases, there is a broadening of the peaks at the regions corresponding to the interfaces (*i.e.*, in Fig. 2.2(b) there is a broadening at the back edge of the peak corresponding to (Ag+ITO) and the front edge of the Si peak). In the case of ZnO (as shown in Fig. 2.3(b)) there is a broadening of the back edge of the Ag peak and the front edge of the ZnO peak. There is also a slight broadening of the front edge of the Si peak.

Figure 2.4 shows the pole figure profile of (111) texture with the intensity plotted against the tilt angle ψ for 45 nm Ag films on ITO and ZnO: as deposited, and for samples annealed at 400 ^oC and 600 ^oC. The intensity peak at $\psi = 67^o$ corresponds to the {111} planes which are at 70.5^o to the surface normal. The twinning related (511) texture[13] can be seen at ψ =

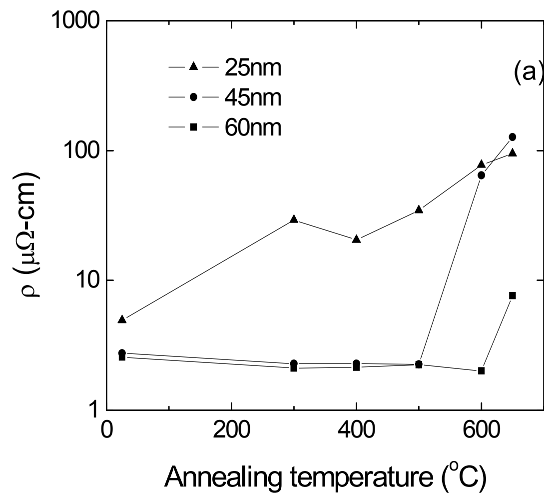

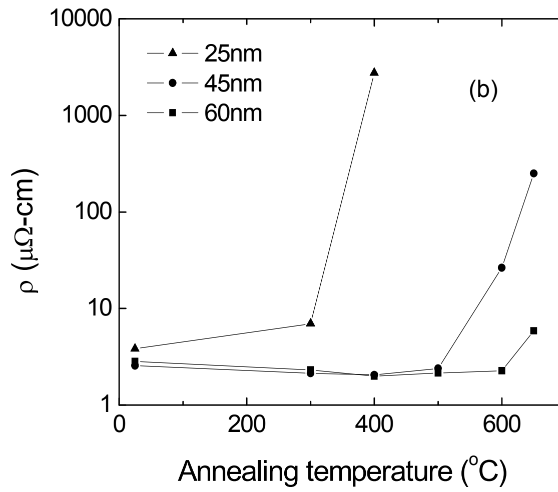

FIG. 2.1: Electrical resistivity of Ag of various thicknesses on: (a) ITO and, (b) ZnO as a function of annealing temperature.

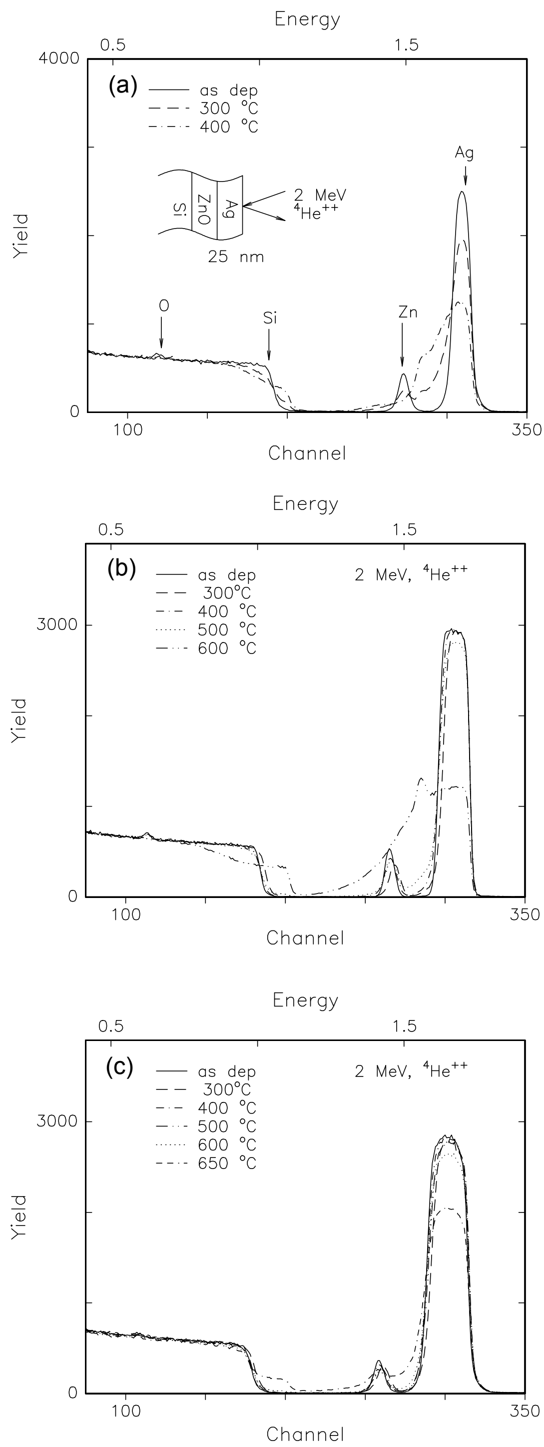

FIG. 2.2. 2.0 MeV RBS spectra for: (a) 25 nm, (b) 45 nm, and (c) 60 nm Ag films on ITO.

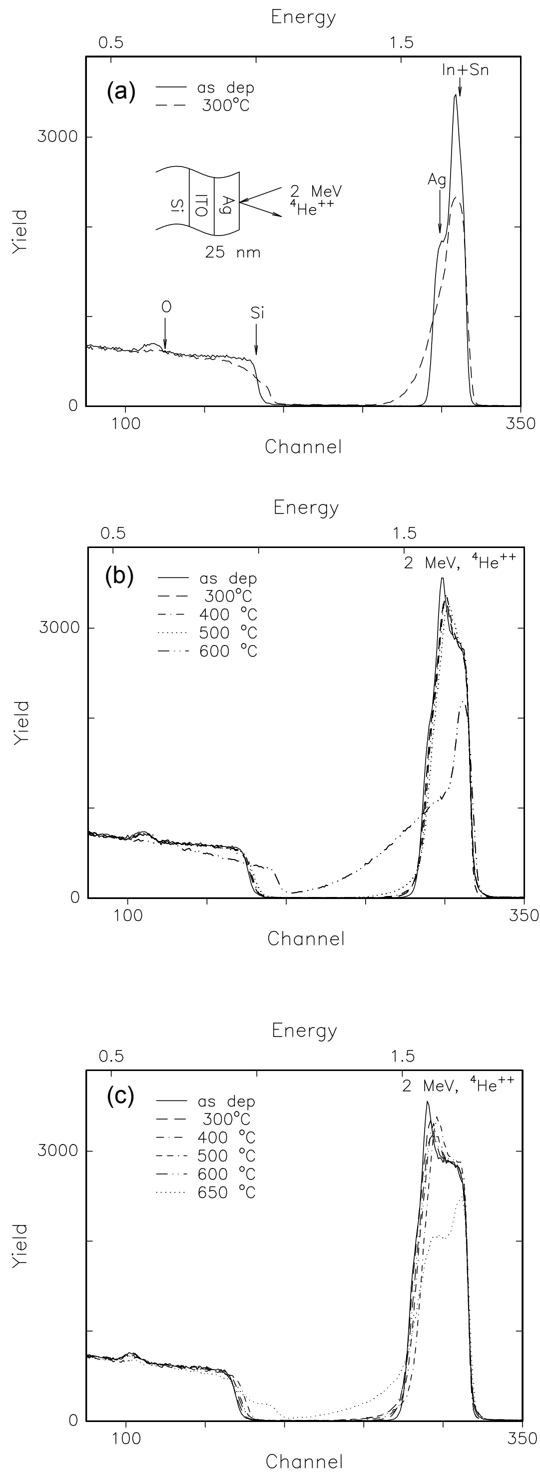

FIG. 2.3. 2.0 MeV RBS spectra for: (a) 25nm, (b) 45nm, and (c) 60 nm Ag films on ZnO

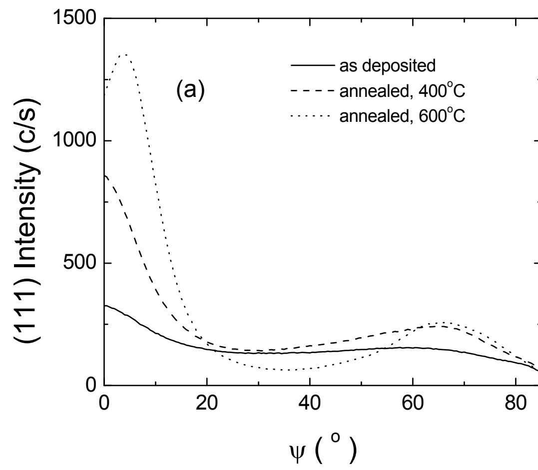

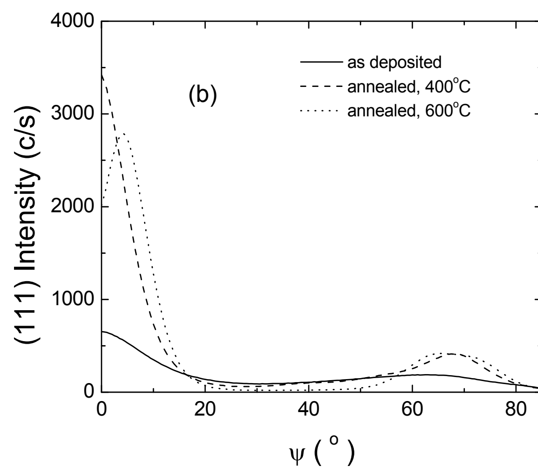

Fig. 2.4. (111) pole figure profiles for 45 nm film of Ag on: (a) ITO and (b) ZnO as deposited, and annealed at 400 °C and 600 °C for 1 h in vacuum.

38.9^o in a plot of the log of intensity with tilt angle ψ in the sample of Ag on ZnO annealed at 400 ^oC. But (200) texture which is usually found to occur in Ag thin films[14,15] at ψ = 54.7^o is not seen in these measurements. The intensity of (111) texture at ψ = 0° is found to increase sharply for the 400 ^oC annealed samples when compared to the as-deposited samples. The 600 ^oC annealed samples have the peak intensity at a value around ψ=7°. Monitoring the [111] Ag peak is a useful method of quantification of the extent of (111) fiber texture. This information is shown in Table 2.I for all the samples of interest.

Figure 2.5 shows the pole figure profiles of (200) texture with the intensity plotted against the tilt angle ψ for 45 nm Ag films on ITO and ZnO: as-deposited, and for samples annealed at 400 ^oC and 600 ^oC. For Ag on both substrates, the greatest increase in pole figure intensity is in the <111> directions at ψ = 54.7^o. For the 600 ^oC annealed samples, there is seen to be a clear increase in <111> intensity and a simultaneous drop in <200> intensity. It is also seen that the drop in intensity of random is much greater for the Ag on ZnO than for the Ag on ITO.

Figure 2.6 represents the three-dimensional (3D) AFM image of the 25 nm Ag film on ITO and ZnO after annealing at 300 ^oC. The average surface roughness of the films increased from 0.7 nm for the as deposited film to 28.3 nm for the Ag on ITO upon annealing at 300 ^oC and from 1.1 nm to 17 nm for the Ag film on ZnO.

Table 2.1: [111] peak parameters from [111] pole figure texture analysis on Ag/ITO and Ag/ZnO samples.

Sample	Background intensity (arb. units)	Height above random (arb. units)	HWHM (arb. Units)
Ag/ITO as-deposited	89	313	15
Ag/ITO 400 ^oC annealed	112	798	10.5
Ag/ITO 600 ^oC annealed	63	1290	7.5
Ag/ZnO as-deposited	42	611	11.5
Ag/ZnO 400 ^oC annealed	36	3383	6
Ag/ZnO 600 ^oC annealed	19	2796	5.5

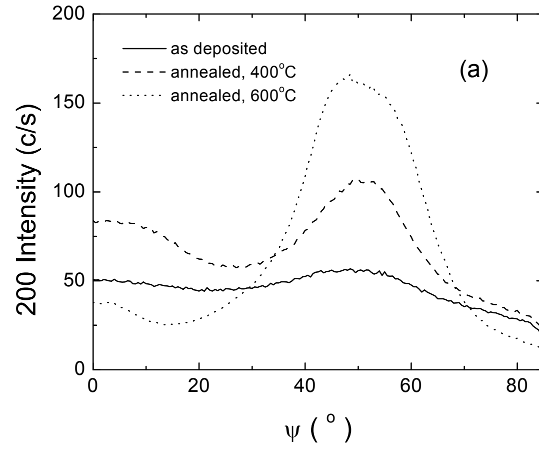

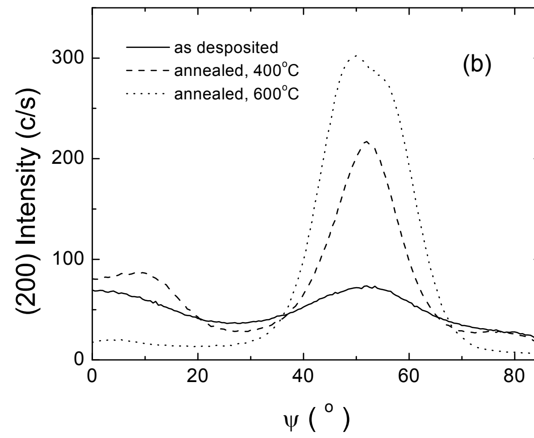

FIG. 2.5. (200) pole figure profiles for 45 nm film of Ag on: a) ITO and b) ZnO as deposited, and annealed at 400 ^oC and 600 ^oC for 1 h in vacuum.

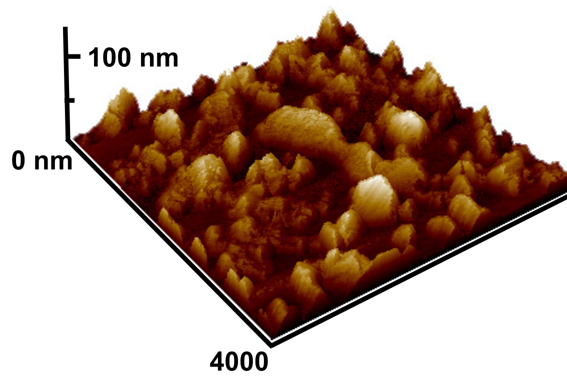

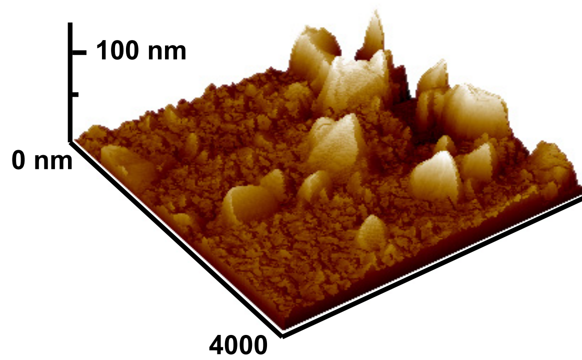

FIG. 2.6. 3D AFM image of 25 nm of Ag film on a) ITO and b) ZnO substrates.

2. 4. DISCUSSION

Changes in resistivity of the Ag films can be understood from the following equation[16]:

$$\rho = \frac{1}{ne\mu} \tag{2.1}$$

ρ is the resistivity, n is the number of charge carriers, e is the charge on the carrier, and μ is the mobility. As can be seen from Eq. 2.1, changes in mobility of the electrons in the film lead to changes in resistivity. In general, the mobility can be stated as:

$$\frac{1}{\mu} = \frac{1}{\mu_i} + \frac{1}{\mu_l} + \frac{1}{\mu_g} \tag{2.2}$$

μ_i represents interface or surface scattering, μ_l accounts for lattice scattering and μ_g for scattering at the grain boundaries. The effect and extent of these various scattering mechanisms must be taken into account to determine the changes in resistivity in a material. As can be seen from Eq. 2.2, it is the dominant scattering mechanism that determines the over all mobility and hence the resistivity. The decrease in resistivity with increasing Ag film thickness is likely due to reduced interface scattering.

However, the resistivity decrease is lesser with increase in Ag film thickness due to a decreasing effect of interface scattering as the resistivity values approach closer to the bulk resistivity value (1.6 μm-cm[17]) of Ag.

The sudden increase in resistivity of the 300 ^oC annealed 25 nm films of Ag is likely due to rapid agglomeration of the Ag in order to reduce its free energy.[18] The process of agglomeration reduces the surface-to-volume ratio at the same time leading to the formation of a discontinuous film. The higher resistivity of the as-deposited 25 nm film of Ag is also suggestive of a near discontinuous film. The discontinuity leads to potential barriers in the electron conduction path, thus increasing the resistivity. Unlike the 25 nm films, the 45 nm films show a significant change in resistivity only at 600 ^oC. Given the surface diffusion induced agglomeration of the films, the greater thickness ensures a continuous path for conduction of the electrons up to 500 ^oC. In the same manner, the 60 nm films of Ag were stable up to 600 ^oC and began degrading only at 650 ^oC. In the Ag films of 45 nm and 60 nm thickness there is also the possibility of degradation by sublimation at the high temperature of 600 ^oC, apart from the process of agglomeration.[13]

Backscattering measurements on the 25 nm films of Ag on ITO and ZnO show a drop in intensity of the Ag peak upon annealing. The reduced intensity in channel numbers 290 to 320 is indicative of an agglomeration process that leads to the formation of exposed regions. This gives rise to a reduced Ag signal in the RBS spectrum. This is illustrated schematically in Fig. 2.7. At a temperature of 300 ^oC, which is considerably less than the melting point (961 ^oC[19]) of Ag, the effect of the sublimation is negligible and the drop in intensity of the RBS signal can be assumed predominantly

to be due to agglomeration. Thus agglomeration occurs immediately on the onset of annealing rendering the films useless for low resistivity applications. However for the 45 nm films of Ag on ITO and ZnO, the RBS signal degrades only at 600 ^{o}C. The reduction in the scattered beam intensity attests to the occurrence of agglomeration; though, the possibility of sublimation cannot be completely ruled out due to the high temperature of anneal.[13] Further, the peaks of Ag, ITO, ZnO, and the Si interfaces are broadened in this structure suggesting more inter-diffusion than for Ag films of 25 nm thickness annealed at 300 ^{o}C. The samples with 60 nm of Ag film on either substrate showed good stability even at 600 ^{o}C and degradation begins only at 650 ^{o}C. Hence, the application temperatures of interest will determine the optimized Ag film thickness to be used.

Figure 2.4 shows the <111> pole figure measurements on silver. For the as deposited samples, the highest intensity is observed for the (111) Ag planes at tilt angle $\psi = 0^{o}$ indicative of preferred orientation of the silver. This is consistent with the lower surface energy associated with this plane.[20] The shift in (111) peak position observed from $\psi = 70.5^{o}$ to $\psi = 67^{o}$ is due to an inaccurate defocusing correction at large tilts.[21] The sharp increase in intensity of (111) texture for the 400 ^{o}C annealed samples, as compared to the as-deposited samples is due to the higher thermal energy of the Ag atoms causing diffusion to attain lowest free energy configuration for the system. The (111) intensities of the as-deposited samples of Ag on

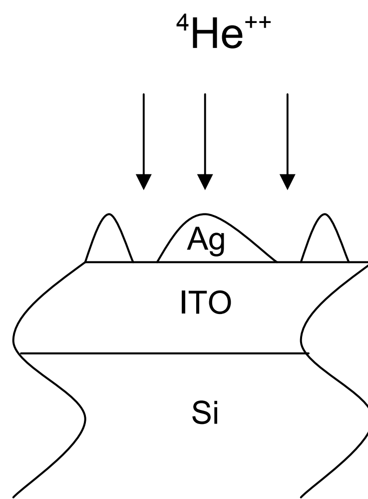

FIG. 2.7. A schematic illustration of self-assembled Ag-island formation and the consequent reduction of backscattered ion intensity.

amorphous ITO and ZnO are comparable, but the intensity is increased for the Ag on ZnO compared to the Ag on ITO in the 400 ^{o}C annealed samples (see Table 2.1). This suggests that the formation of crystalline ZnO with the hexagonal lattice strongly favors (111) nucleation and growth of the Ag. This is because crystalline ZnO has a strong preference for (001) orientation [22], with its *c*-axis normal to the surface. The 6-fold symmetry of the (001) ZnO planes greatly enhances (111) plane texturing of the Ag films which have 3-fold symmetry. In contrast, ITO crystallizes into a BCC structure and is not as conducive for the formation of these (111) planes. The background intensity in the plot is a measure of the degree of random orientation in the film, which has been quantified by the minimum in the ψ plot [15] tabulated in Table 2.1. It is interesting to note that in the case of Ag on ITO there is an increase in intensity at all ψ values for the 400 ^{o}C annealed sample when compared to the as-deposited sample. This indicates an overall increase in crystallinity in the former. On the other hand, in the case of ZnO, the degree of random orientation is less in the 400 ^{o}C annealed sample than in the as-deposited sample. For the 600 ^{o}C annealed samples on both ITO and ZnO, one can observe a decrease in background intensity when compared to the as-deposited samples, due to the formation of enhanced (111) texture. Further, the Ag films have the peak slightly shifted from $\psi = 0^{o}$ to about $\psi = 7^{o}$. This could be either due to the formation of a near-<111> fiber texture[23,24] or the agglomerated islands having an uneven surface. The

latter appears to be the more likely phenomenon due to the lack of motivation for the formation of a near-<111> Ag texture on top of BCC structured ITO. Hence, it is speculated that the shift in the position of the [111] peak must be due to the Ag island formation. [25]

Additional studies on the texturing behavior of the Ag utilized (200) pole figures to further confirm an increase in the degree of randomly oriented grain growth in the case of Ag on ITO. However for Ag deposited on ZnO, despite an increase in crystallinity in specific directions such as [111] at $\psi = 54.7^o$, the overall degree of random orientation seems to have reduced. This suggests that the ZnO substrate favors Ag growth in specific directions; whereas, ITO merely serves as a passive substrate. The maximum increase in crystallinity is in the [111] direction for both samples. A shift of the (111) peak location is seen in the (200) pole figures for 600 ^oC annealed samples of Ag on both ITO and ZnO. This is likely due to the island formation of the Ag films.

Thus the texturing of Ag on ZnO is determined by the following two factors : i) the tendency for Ag to favor (111) orientation based on surface energy considerations, and ii) the tendency for ZnO to favor (111) orientation of Ag based on interface energy consideration. In the case of Ag on ITO only the former plays a role and hence the degree of texturing is reduced.

The as-deposited samples of Ag on both substrates have an average

surface roughness that varies between 0 to 2 nm for different thicknesses. Immediately upon annealing however, there is at least a five-fold increase in roughness. The 3-D AFM images shown in Fig. 2.6 of the 300 ^{o}C annealed 25 nm film of Ag on ITO and ZnO clearly shows the formation of Ag islands upon annealing, characteristic of a discontinuous film. [23] The resistivity of the 25 nm films of Ag increases upon annealing due to severe agglomeration; however in all the other films, the resistivity improves initially upon annealing, and suggests an improved crystallinity.

Agglomeration on annealing is to be expected in films which have a close lattice mismatch with the substrate because of the unstable equilibrium in which the system exists. Figure 2.8 shows an Arrhenius plot of agglomeration of the 45 nm films of Ag on ITO and ZnO. The agglomeration has been modeled using the Ostwald ripening theory.[26] This theory can be used to predict both the power-law dependence and the temperature dependence of the growth rate.

The temperature dependence for island growth can be described by:

$$K = (K_o / T)\exp(-E_A / k_B T) \qquad (2.3)$$

K is the rate of change in the mean island size with time and E_A represents the activation energy for diffusion. The applicability of the Ostwald theory is tested by plotting the growth rate dependence on temperature. The term $\ln(T * R_{av}^3 / t)$ on the ordinate is a logarithmic measure of the volume growth

rate of the Ag islands as approximated using the cube of the root-mean-square roughness (R_{av}). The additional temperature factor on the ordinate is due to the Ostwald ripening approach which predicts an $[\exp(-E_A / k_B T)]/T$ dependence for the ripening.[27] Figure 2.8 shows that the third-power dependence of the average roughness of the films (as measured using AFM) varies linearly with time up to 500 ^{o}C before increasing at a greater rate. Using Eq. 2.3, activation energy was determined from the slope for the linear part of the curve. The activation energies for diffusion of Ag on ITO and ZnO films have been calculated to be 0.62 ± 0.8 eV and 0.36 ± 0.6 eV, respectively. Beyond 500 ^{o}C there is an increase in the rate of agglomeration. This might be due to the onset of lattice diffusion as it is known that initial agglomeration happens by surface diffusion related grooving in Ag [28] and that volume diffusion has a larger onset time. [29]

Based on the resistivity data, x-ray pole figure analysis of texturing and crystallinity, and AFM measurements, the initial decrease in resistivity of the Ag films on both ITO and ZnO substrates with anneal temperature is due to better crystalline quality of the layers. The decrease in resistivity however is not in proportion to the increase in crystallinity as this is offset by the increase in average surface roughness as seen in AFM measurements (see FIG. 2.7). Beyond a certain anneal temperature, the surface roughness effect starts to dominate and the resistivity rises again. Hence, it can be

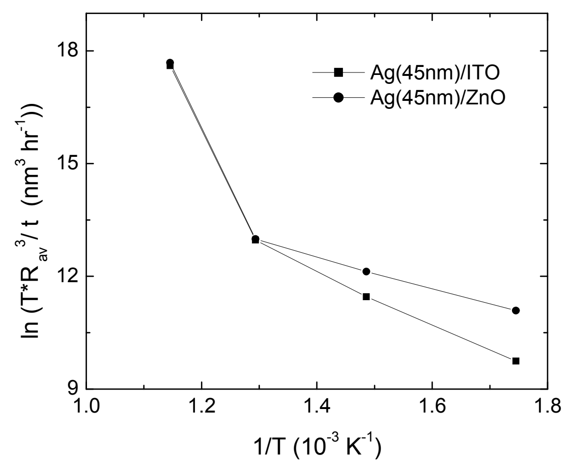

FIG. 2.8. Arrhenius plot of agglomeration of the 45 nm films of Ag on ITO and ZnO.

seen that the variation of the overall resistivity with anneal temperature is determined by the combined and counterbalancing effects of increasing crystallinity and surface roughness.

2. 5. CONCLUSION

This study investigates island formation and texture evolution of Ag films deposited on to ITO and ZnO. Island formation has been inferred from RBS data. AFM roughness measurements combined with texture measurements account for the resistivity changes of the Ag films upon annealing. Pole figure data also reveal a greater texture enhancement for the Ag films on ZnO substrate due to minimization of surface and interface energies. Ostwald ripening theory is used to explain the agglomeration behavior of the Ag films. This understanding of the high temperature processing behavior of Ag films on transparent conducting oxides is advantageous for the use of Ag and its alloys in optoelectronic applications including solid-state photovoltaic devices on flexible substrates.

CHAPTER 3

THE ROLE OF COPPER IN ZnO/Cu/ZnO THIN FILMS FOR FLEXIBLE ELECTRONICS

3. 1. INTRODUCTION

Transparent conducting oxides (TCOs) are a class of materials that can exhibit simultaneous conductivity and transparency though these properties are usually mutually exclusive.[1] This behavior makes TCOs useful for a wide range of practical applications including in flat-panel displays (*e.g.*, liquid crystal displays used in the optoelectronics industry), solar cells, gas sensors, thin film resistors, photovoltaic devices, organic light emitting diodes (OLEDs), smart windows, and electromagnetic shielding of cathode ray tubes used for video display terminals.[2-4] Other common applications include optical filters, heat mirrors, low emittance films for advanced glazing, and protective or decorative coatings.[5] Indium tin oxide (ITO) is the commonly preferred choice of industry because of its high electrical conductivity (10^4 $\Omega^{-1}cm^{-1}$) combined with high transmittance (>80%) in the visible spectral range[6]; however, indium is very rare and costly (almost US$1400/kg).[5] This makes ITO a non-viable choice for mass, large-scale economical production in the future.[7] As a consequence, there is a need for alternative commercially viable TCOs.

Doped zinc oxide (ZnO) films are known to exhibit good electrical

conduction and optical transmission in the visible region.[7-9] Recently, some groups have realized sufficiently low resistivity (1-2 $\times$ 10^{-4} Ω-cm) and high transmittance (above 80% in the visible range) using gallium-doped zinc oxide films.[10, 11] Indium-doped zinc oxide has also been reported to be an ideal transparent conducting oxide material for optoelectronic devices, solar cells, and organic LEDs, due to a large work function, a wide transmittance window from 400 to 2500 nm, and a higher chemical etching rate compared to ITO thin films. [12] ZnO has practical advantages of availability of inexpensive large-area substrates and good radiation resistance.[13, 14]

Although doped-ZnO films have shown good conduction and transmission characteristics, there is an inherent limitation to the increase in conductivity that can be obtained by increasing the carrier concentration because of ionized impurity scattering. Due to this disadvantage, TCOs with sufficiently low sheet resistance and transparency are still unavailable for many applications.

Dielectric-metal-dielectric thin films have been studied in the hope of increasing conductivity without significant losses in transmission.[15,16] Various studies have been done using silver as the sandwiched metal layer[7,16,17] because Ag has the lowest resistivity of all metals. Copper has a comparable resistivity; hence, there are also studies documenting the resistance and transmission properties of ZnO multilayers with copper.[18,

19] However, there is a lack of investigations addressing the role of copper's impact on carrier concentration and mobility. There is also a lack of detailed understanding of the role of copper in affecting the optical properties of the films.

Recent developments in the area of microelectronics on flexible substrates have generated substantial interest since flexible substrates can overcome the disadvantages of glass (heavy weight, brittle) substrates for application in mobile electronics. A good flexible substrate should be lightweight, dimensionally stable, resistant toward moisture and oxygen, thermally stable, tough, chemically resistant, and have a low coefficient of thermal expansion. [6] Polyethylene terephthalate (PET), polyethylene napthalate (PEN) and polycarbonate are being widely researched as substrate materials for flexible displays. In this study, we report obtaining ZnO/Cu/ZnO multilayer structures with very high conductivities by magnetron sputtering at room temperature on flexible PEN substrates, while retaining transmittance values acceptable for optoelectronic applications. The conduction mechanism as a function of copper thickness and the role of the copper layer in influencing conduction behavior has been investigated. The transmission properties of the films are also investigated to understand the role of copper in influencing the transmission spectrum.

3. 2. EXPERIMENTAL

Zinc oxide thin films have been fabricated by using various methods

such as magnetron sputtering, spray pyrolysis, chemical vapor deposition (CVD), sol-gel technique, pulsed laser deposition (PLD), evaporation, and molecular beam epitaxy. Among them, magnetron sputtering is widely used for fabricating thin films because it has advantages such as ease of large-area deposition, low deposition temperature, high deposition rate, good adhesion between film and substrate, good surface uniformity, and simple equipment.[7] Hence magnetron sputtering was used in the preparation of the samples. The base pressure prior to deposition was approximately $1x10^{-7}$ Torr. Substrate to target distance was 6 cm and was maintained at the same value for all experiments. Thin films layers of ZnO and Cu were deposited onto flexible PEN substrates at room temperature. There was no break in vacuum at any stage during the preparation of the films. Both top and bottom ZnO layers were approximately 30 nm thick; copper thicknesses were varied between 3 nm and 8 nm. Bare ZnO layers without any copper were also prepared under identical conditions for comparison of properties. The ZnO was sputtered at 10 mTorr argon pressure using 100 W RF power. Copper was deposited using 10 mTorr argon pressure and 40 W DC power. The sputtering targets used in this study were 99.999% pure ZnO, and 99.99% Cu and were presputtered for 10 minutes prior to growth.

Rutherford backscattering spectrometry (RBS) was used to determine the thickness of the films. The analysis was performed in a vacuum of 10^{-6} Torr using a 2.0 MeV He^{++} ion beam and total accumulated

charge of 20 μC in a General Ionex Tandetron accelerator. Sample and detector were in the Cornell geometry such that the backscatter detector is directly below the incident beam. The samples were tilted to 45° off normal incidence to increase the depth resolution. Energy spectra were obtained using a surface-barrier detector and were analyzed using the RUMP computer simulation program.[20] Transmission electron microscopy (TEM) using a Philips CM200-FEG TEM operating at 200kV was used to confirm the thickness of the Cu midlayer and study the continuity of the metal layer.

Electrical resistivity, Hall mobility, and carrier concentration of the films were measured by Hall measurements in the van der Pauw geometry using an Ecopia HMS-3000 instrument. Four-point-probe analysis, to determine the sheet resistance, was carried out using a Keithley 2700 data acquisition system.

Optical transmittance and reflectivity were measured using an Ocean Optics double channel spectrometer (model DS200) in the wavelength range 300-900 nm with an aluminum mirror as the reference for reflectivity and a bare PEN substrate for transmittance. Tungsten-halogen and deuterium lamps were used for the visible and UV light sources, respectively.

In an effort to determine the chemical state of the buried metal layers, XPS sputter depth profiles were obtained using a Physical Electronics Quantera XPS microprobe. XPS spectra were acquired using a focused,

monochromatic, Al kα x-ray beam that was adjusted to be 200 μm in diameter. Analyzer pass energy of 69 eV was used to provide the energy resolution required to identify the chemical state of the buried metal layers. Sputter etching was accomplished using a 1 keV argon ion beam that was rastered over a 3x3 mm area to provide a flat crater bottom. Using these conditions, the sputter etch rate for an SiO_2 thin film reference sample was approximately 1.25 nm/min. The sputter interval was 1 minute and the sample was rotated azimuthally about the analysis point during sputtering to minimize accumulation of sputter induced artifacts that could degrade layer definition during the measurement. Since the thin films were deposited on an insulating substrate, the instrument's charge neutralizing apparatus was used. The apparatus provides low energy (1 eV) electrons and low energy (8 eV) ions to neutralize the sample surface. Data reduction was performed using PHI MultiPak.

The role of crystallinity in the ZnO layer was studied by X-ray diffraction in the Bragg-Brentano configuration (θ-2θ geometry) and pole-figure analysis using a Philips X'pert multipurpose diffractometer system. Cu Kα radiation was used for the incident X-ray beam. The operating voltage and filament current were 45kV and 40mA, respectively. The Bragg-Brentano scan collects X-rays diffracted from {*hkl*} planes parallel to the substrate surface. This technique has been used to observe the extent of crystallinity of the ZnO layers. Pole-figure analysis, on the other hand,

provides texture information for polycrystalline thin films, both quantitatively as well as qualitatively, as a function of sample tilt. The evolution of (002) ZnO texture with increasing Cu midlayer thickness has been studied by one-dimensional pole figure analysis, which measures the intensity of x-rays diffracted from the sample as a function of tilt angle, ψ. The sample tilt (ψ) was varied from 0° to 85°.

Annealing of the samples was done in a reducing atmosphere ($Ar+5\% H_2$) at 150 ^oC for up to 24 hours.

3. 3. RESULTS

Figure 3.1 shows a representative glancing angle XRD profile from one of the ZnO/Cu/ZnO multilayer films. The high peaks labeled "S" are X-ray peaks from the substrate. The tiny peak at 34.4^o corresponds to the ZnO (002) set of planes, based on JCPDS card no. 89-1397. The low intensity of this peak indicates that the ZnO layers are mostly amorphous.

Figure 3.2 shows the variation of resistivity of the ZnO/Cu/ZnO films as a function of the thickness of the copper layer. It is known that as-deposited ZnO films can vary greatly in their resistivity.[21-23] For the as-deposited ZnO films in this study, the resistivity was 0.46 MΩ-cm for 60 nm of ZnO. For the ZnO/Cu/ZnO structures on PEN, the resistivity decreases drastically from 0.46 MΩ-cm for 0 nm of Cu thickness to 3.87×10^{-5} Ω-cm at 8 nm of Cu thickness. However, it can be seen that the rate of change of resistivity (i.e., the rate at which the resistivity drops) decreases as the

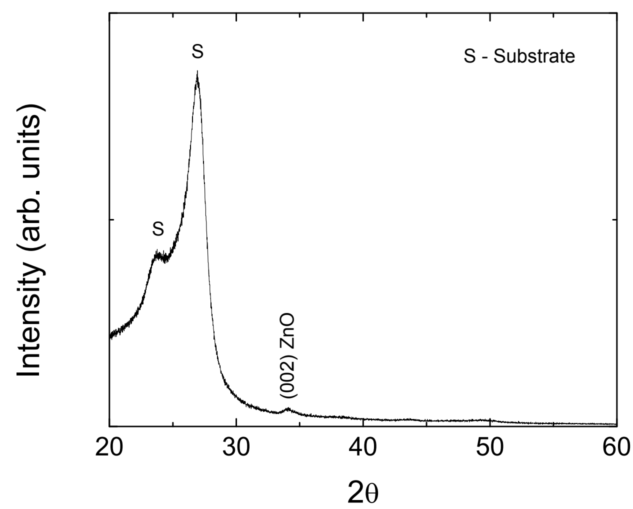

FIG. 3.1. Glancing angle XRD profile showing the largely amorphous structure of ZnO in the ZnO/Cu/ZnO multilayers.

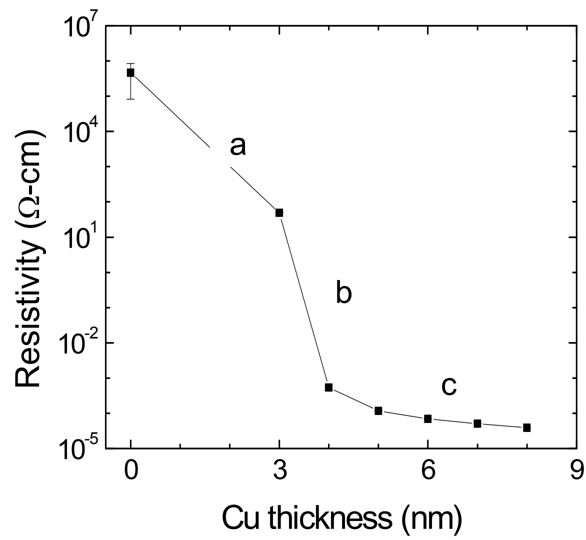

FIG. 3.2. Resistivity of the ZnO/Cu/ZnO thin films as a function of copper layer thickness.

copper layer thickness increases.

Figure 3.3 shows the variation of sheet resistance of the ZnO/Cu/ZnO films as a function of the thickness of the copper layer. The as-deposited ZnO films had a sheet resistance of 6000 MΩ/sq. The sheet resistance, like the resistivity, is seen to decrease dramatically from 6000MΩ/sq. to 3.06 Ω/sq. with increase in thickness of the copper midlayer. It can be seen that the rate of decrease in the sheet resistance also decreases as the copper layer thickness increases. The variation of resistivity and sheet resistance is a consequence of changes in carrier concentration and mobility.

Figure 3.4 shows the variation of carrier concentration in the ZnO/Cu/ZnO films as a function of copper layer thickness. The carrier concentration increases with increasing copper midlayer thickness. The carrier concentration of undoped ZnO on PEN is about 3×10^{13} cm^{-3}. The carrier concentration of the ZnO sandwich structure with 8 nm of Cu is increased by nine orders of magnitude to 1.59×10^{22} cm^{-3}. However, it can be seen that most of the increase happens before the Cu midlayer reaches 6 nm in thickness. Beyond that there is a small rise in carrier concentration up to 8 nm of Cu thickness. Variation of Hall mobility with thickness of the copper layer is shown in Fig. 3.5. The mobility of the as-deposited ZnO films is 2.8 cm^2/V-s. The mobility drops to a low 0.64 cm^2/V-s for films with a 3

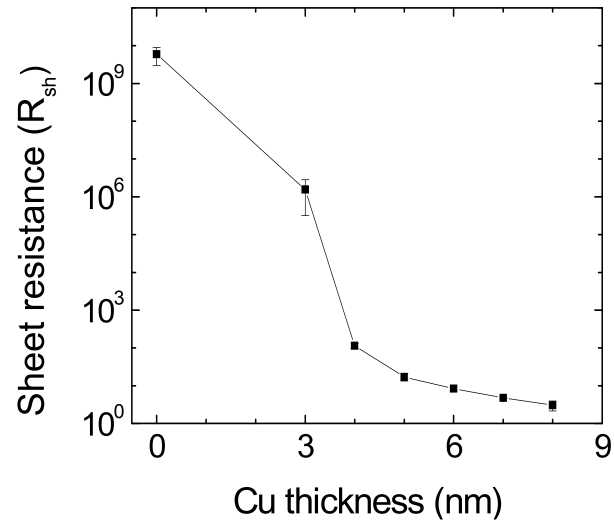

FIG. 3.3. Sheet resistance of the ZnO/Cu/ZnO thin films as a function of copper layer thickness.

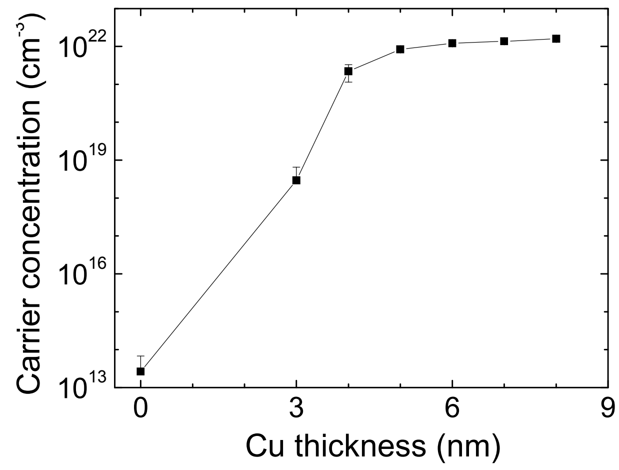

Fig. 3.4. Carrier concentration of the ZnO/Cu/ZnO thins films as a function of copper layer thickness.

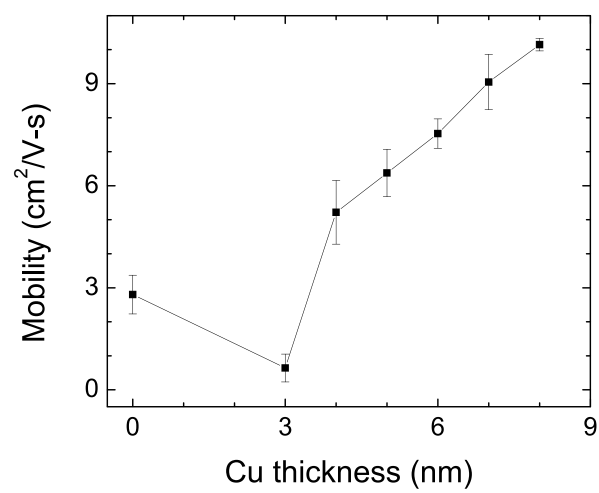

Fig. 3.5. Hall mobility of the ZnO/Cu/ZnO thins films as a function of copper layer thickness.

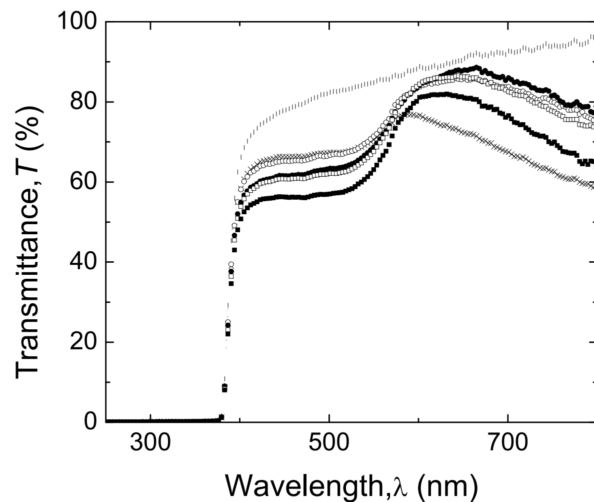

FIG. 3.6. Optical transmittance spectra relative to the PEN substrate for ZnO/Cu/ZnO thin films as a function of Cu thickness for thicknesses of: 0 nm (vertical dash (I)), 4 nm (cross-hatch(x)), 5 nm (open circle (○)), 6 nm (filled circle (●)), 7 nm (open square (□)), and 8 nm (filled square (■)).

nm copper midlayer. Thereafter, the mobility increases with increasing copper midlayer thickness and reaches 10.1 cm^2/V-s at 8 nm of Cu thickness.

Figure 3.6 shows optical transmittance spectra relative to the PEN substrate for ZnO/Cu/ZnO thins films with different copper thicknesses. The optical transmittance of undoped ZnO films is about 90% over the visible range of wavelengths (400 nm – 700 nm). Upon insertion of a copper layer, the photopic average transmittance of the ZnO multilayer drops to between 70 % and 75 %. However, the variation in transmittance with copper thickness is different for shorter wavelengths and longer wavelengths. In the shorter wavelengths near the blue part of the visible spectrum, as the thickness of the copper layer increases, the transmission decreases. In the red wavelengths as the copper layer thickness decreases from 8 nm to 6 nm, the transmission increases. However below this thickness, the transmittance decreases again. It is also observed that there is an increase in transmission with decreasing wavelength in the longer wavelength regions.

Figures 3.7 and 3.8 show the results of XPS analysis of the ZnO/Cu/ZnO samples. Figs. 3.7 (a) and 3.7 (b) show sputter depth profiles for (a) 3 nm, and (b) 8 nm Cu thickness. The apparent depth determined using the sputter time and ZnO thickness was found to be 1.25 nm/min. It is observed that Cu shows 40 % peak atomic concentration in the 3 nm

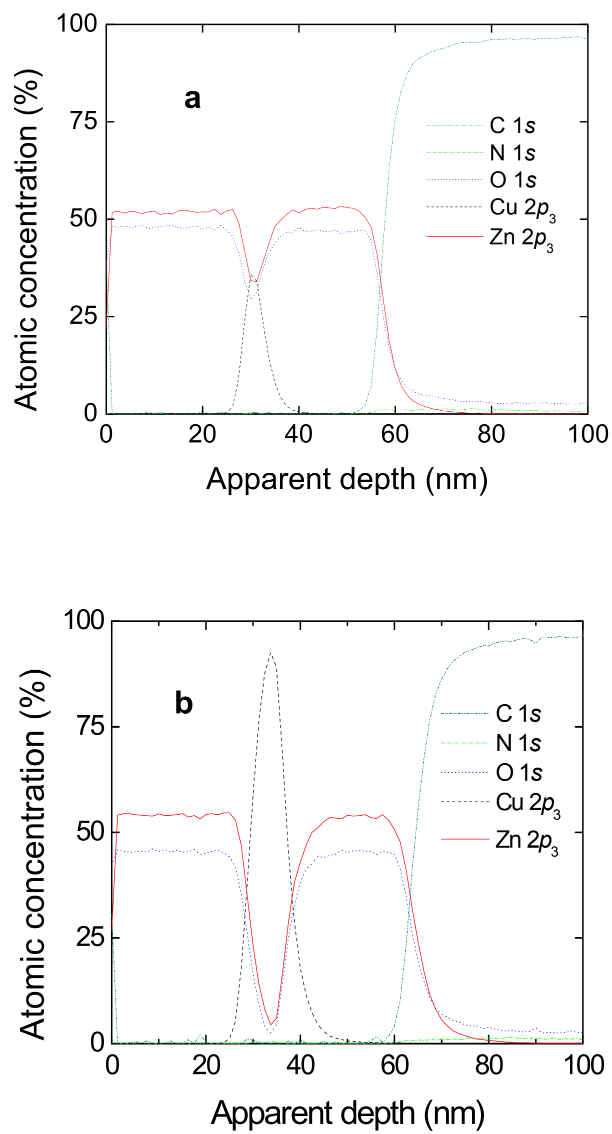

FIG. 3.7. XPS profiles of the ZnO/Cu/ZnO samples showing atomic concentration of the various elements with sputter depth for (a) 3 nm, and (b) 8 nm Cu thickness structures.

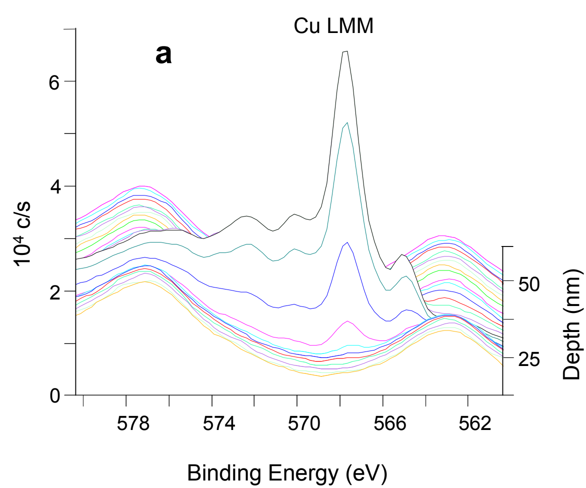

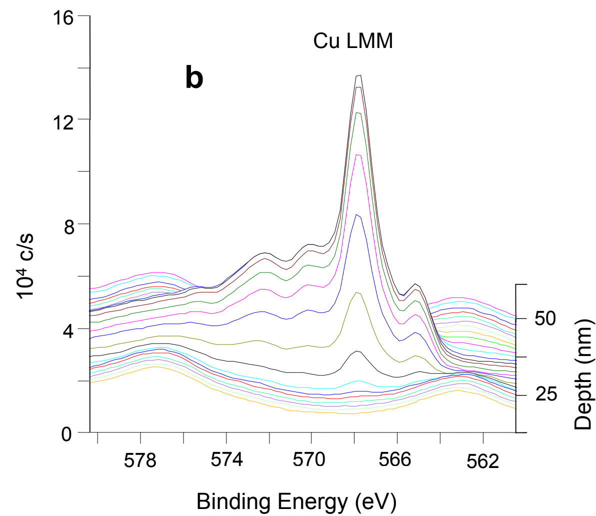

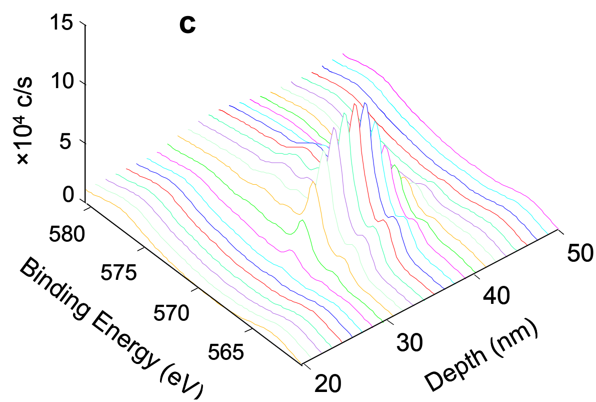

FIG. 3.8. Intensity of Cu LMM line with depth of sputter during XPS for (a) 3 nm, and (b) 8 nm thick Cu layer structures is also shown. The 3-D representation of (b) is shown in (c).

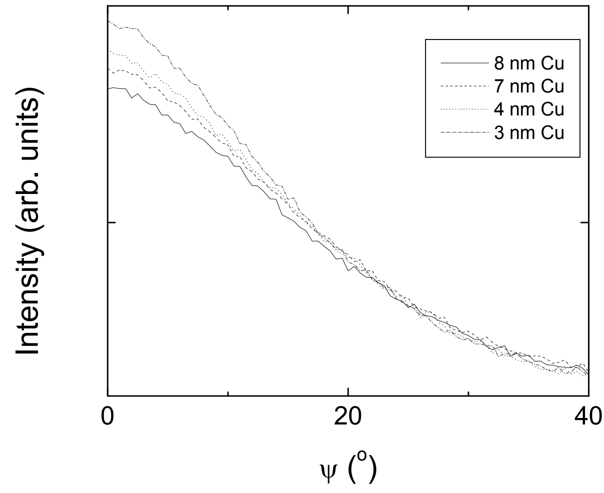

FIG. 3.9. Pole figure profile of ZnO (002) texture showing intensity plotted against angle of tilt, ψ.

thickness film and 93 % peak atomic concentration in the 8 nm thickness films. Figs. 3.8 (a) and 3.8 (b) show intensity of the Cu LMM line for the metallic state of copper (binding energy = 568.2 eV)[24] with depth of sputter for (a) 3 nm, and (b) 8 nm thick Cu films. It can be seen that there is no change in the peak position across the Cu layer in both films. Fig. 3.8 (c) shows a three dimensional representation of the information compressed into Fig. 3.8 (b) to make clear the absence of a shift in peak position.

Figure 3.9 shows a pole figure profile of ZnO (002) texture with intensity plotted against angle of tilt (ψ). The graph shows only up to a tilt, ψ, of 40° although the scan was done up to a tilt of 85° as no other peaks are seen. The two thicker films of 7 and 8 nm Cu thickness have been plotted along with the two thinner films of 3 and 4 nm thickness. It is interesting to note that there is a marginal decrease in texturing with increase in thickness of the copper midlayer.

Figure 3.10 shows transmission electron micrographs of the films. Figure 3.10 (a) shows a micrograph obtained from the multilayer structure with a 3 nm copper midlayer. As can be seen in the figure, the Cu layer is in the form of poorly connected islands. Figure 3.10 (c) shows a TEM image obtained from the multilayer structure with the 8 nm copper midlayer. It can be seen that the islands are contiguous.

Annealing of the films for up to 24 hours in a reducing ambient at 150 ^oC didn't result in any significant change in conduction and

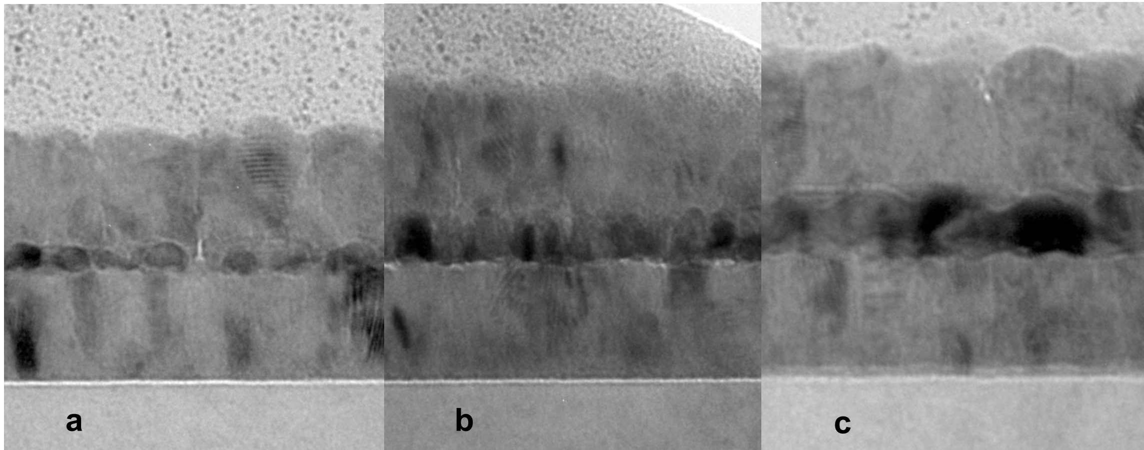

FIG. 3.10. Cross-section TEM micrographs of ZnO/Cu/ZnO films with varying Cu thickness: (a) 3 nm, (b) 6 nm, and (c) 8 nm.

transmittance properties of the films. However, PEN cannot be taken to higher temperatures and held for long times without risk of damaging the substrate.

3. 4. DISCUSSION

Discontinuous metal films tend to form during sputter deposition of very low thickness metal films leading to high resistivity samples. [25] The resistivity decreases gradually with increasing thickness for the multilayer structures with copper film thickness less than 3 nm, as shown in region (a) of Figure 3.2. Carrier injection or thermionic emission and conduction through the dielectric dominate when the metal islands are small andseparation between islands is large.[26] As the islands grow, the gap between the islands reduces and some of the islands undergo large scale coalescence.[27] This leads to a drastic reduction in resistance as observed in region (b) of Figure 2. Bulk conduction takes place through the coalesced islands and a process of activated tunneling occurs between the larger islands with small gaps between them.[28] The conductivity in this regime is governed by the equation[29]:

$$\sigma \propto \exp(-2\beta s - \frac{W}{kT}) \tag{3.1}$$

where β is the tunneling exponent of electron wavefunctions in the insulator, s is the island separation, W is the island charging energy, k the Boltzmann constant, and T is the temperature. As can be seen from

equation (3.1), the spacing between the islands and the size of the islands, which affects the island charging energy W , play a critical role in determining the overall conductivity. After the large scale coalescence occurs, there is a transition from discontinuous copper islands dispersed in a dielectric matrix to a contiguous film with holes. This corresponds to region (c) in Figure 3.1. The formation of this near-continuous film by about 6 nm of copper thickness can also be inferred from the jump in mobility to about 8 cm^2/V-s as shown in Figure 3.5. In the neighborhood of the transition, the curve resembles a hyperbola if the islands and bridges grow at the same rate.[30] The network film becomes a continuous film through the filling of the voids. Nucleation takes place in the voids and the new grains are incorporated in the film. [31] At this stage, the main contribution to the resistance comes from diffuse scattering of the conduction electrons at the Cu-ZnO interfaces, grain boundaries, and defects. [32] The mobility in this region can be seen to increase gradually with thickness due to reduction of interface scattering and nominal grain growth. The measured carrier concentration, shown in Figure 3.4, increases linearly with thickness consequent to the contribution of the valence electrons of copper for conduction.

A figure of merit, φ_{TC}, has been estimated for the films, defined as [33]:

$$\varphi_{TC} = \frac{T_{av}^{10}}{R_{sh}} \tag{2}$$

where T_{av} is the average transmittance and R_{sh} is the sheet resistance. The average transmittance was determined by using the equation:

$$T_{av} = \frac{\int V(\lambda)T(\lambda)d\lambda}{\int V(\lambda)d\lambda} \quad (3)$$

where $T(\lambda)$ is the transmittance and $V(\lambda)$ is the photopic luminous efficiency function defining the standard observer for photometry.[34] This choice is in keeping with the application of these films to flexible display devices. Although the figure of merit obtained by using this transmittance value might be lesser than that obtained using the peak value of transmittance, or the linearly averaged value of transmittance as is usually done, this approach gives a more realistic estimate of the actual merit of the film for display device applications. This is based on the fact that the photopic function is a measure of the sensitivity of the human eye. The figures of merit thus obtained are shown in Table 3.1. As can be seen from these values, the best figure of merit is obtained when the copper layer is just continuous to electron conduction.

Figure 3.6. shows optical transmittance spectra relative to the PEN substrate for the films. As can be observed, there is a drop in the photopic averaged optical transmittance from about 90% for the undoped ZnO films to between 70 and 75% when there is a thin copper layer in between. However, the variation in transmittance with copper thickness is different in

Table 3.1. Haacke figure of merit for the multilayer films with different copper thicknesses.

Cu thickness (nm)	Transmittance (T)	T^{10}	Sheet resistance (R_{sh} Ω/sq.)	$\varphi_{TC} = \frac{T_{av}^{10}}{R_{sh}}$ (Ω^{-1})
4	0.720	0.03743	113.6	0.0003
5	0.750	0.05631	16.5	0.00341
6	0.751	0.05706	8.3	0.00683
7	0.727	0.04124	4.7	0.00870
8	0.689	0.02411	3.0	0.00787

the short and long wavelengths. In the short wavelengths near the blue part of the visible spectrum, as the thickness of the copper layer increases the transmission decreases. In the blue part of the spectrum, the reflectance of copper is low. Transmission is primarily affected by absorption of light due to interband electronic transitions, in particular, due to the excitation of electrons from the *d*-band to the Fermi surface.[35] With increased copper layer thickness, there are more bound electrons available for excitation leading to a greater drop in transmittance. In the red wavelengths as the copper layer thickness decreases from 8 nm to 6 nm, the transmission increases. However below this thickness, the transmittance decreases again. This is because in the red part of the visible spectrum, copper films are reflective.[36] For the film with the 8 nm copper midlayer, the transmittance is low due to high reflectance in red part of the spectrum. As the copper layer thickness decreases from 8 nm to 6 nm, there is lesser reflectance and hence increased transmission. However, below this thickness, the transmittance decreases again because the presence of discontinuous copper islands leads to significant scattering losses. The optical transmittance results therefore further confirm the inference of formation of a contiguous copper conduction layer at 6 nm of Cu thickness arrived at based on conduction behavior. It is also observed that there is an increase in transmission with decreasing wavelength in the longer wavelength regions. Free carrier absorption is significant at longer

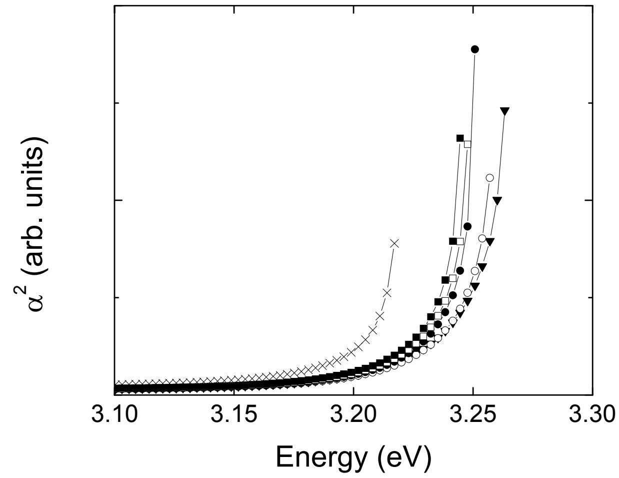

FIG. 3.11. Plot of absorption coefficient versus energy of photons showing the Burstein-Moss effect in the ZnO/Cu/ZnO multilayer films with increasing copper thickness for thicknesses of: 0 nm (cross-hatch(x)), 4 nm (filled square (■)), 5 nm (open square (□)), 6 nm (filled circle (●)), 7 nm (open circle (○)), and 8 nm (filled triangle (▼)).

wavelengths. [35,37] However, the screening effect of the bound electrons leads to an increase in transmission with decreasing wavelength in the wavelengths beyond 580 nm, which is known to be the crossover point.[35]

Figure 3.11 shows the change in absorption coefficient with incident energy for the multilayer films with varying copper thicknesses and for the ZnO on PEN without any copper. To determine the energy gap E_g, the following relationship is used:[38]

$$\alpha(h\nu) \propto (h\nu - E_g)^{1/2} \quad (3.4)$$

where $h\nu$ is the photon energy and α is the absorption coefficient. The optical band gap is deduced from the absorption edge by linear extrapolation back to zero. ZnO is reported to have an optical band gap of ~3.2-3.3 eV.[39, 40] The optical band gap obtained from Fig. 3.11 is ~3.21 eV. Although this value is within the range for ZnO band gap, it is more advantageous to utilize the combined band gap of the ZnO+PEN structure because PEN is known to have a band gap of ~3.2 eV.[6] From Fig. 3.11 it is evident that the band gap of the ZnO films undergo a blue shift with increasing thickness of the copper layer. The increase in carrier concentration with increased copper thickness leads to a filling of the small density of states of ZnO near the conduction band minimum.[41] Hence, there is a shift in the absorption edge to higher energies, known as the Burstein-Moss effect. [42]

Figures 3.7 (a) and 3.7 (b) show XPS profiles depicting the variation

in atomic concentration of elements across the depth of the multilayer structures with 3 and 8 nm Cu midlayer thicknesses respectively. It can be seen in Fig. 3.7 (a) that the multilayer structure with 3 nm Cu shows only 40% presence of Cu in the Cu thin film region, with the rest being Zn and O. Fig. 3.8 (a), which shows the Cu LMM line with peak binding energy of 568.2 eV corresponding to the metallic state of copper, indicates that the Cu is present almost entirely as Cu metal across the depth of the copper layer as there is no change in the position of the Cu peak. The position of the Cu LMM line corresponding to Cu_2O is 570.1 eV. Thus, Figure 3.8 (a) makes it evident that the copper is not oxidized but present in its purely metallic state. However, Fig. 3.7 (a) suggests considerable presence of Zn and O in the regions containing copper. So the copper is probably in the form of metallic islands with ZnO filling up the spaces between the copper islands. Fig. 3.7 (b) shows the XPS depth profile from the 8 nm copper thickness multilayer. There is up to 93% Cu presence in the Cu film region suggesting that the layer is contiguous with marginal ZnO presence due to uneven continuity across the entire Cu/ZnO interface. Fig. 3.8 (b) confirms that the Cu is in the metallic state throughout the layer as there is no shift in the XPS peak position corresponding to metallic copper. Thus, the XPS results confirm the inference of formation of Cu islands with poor connectivity at lower thicknesses and the presence of a contiguous copper layer providing a continuous metallic conduction pathway at higher Cu thicknesses. The XPS

also proves that the copper is unoxidized. This can be easily visualized using Figure 3.8 (c).

It is interesting to note that in the ZnO (002) pole figures shown in Figure 3.9, when the copper midlayer is thicker (7 and 8 nm), the degree of texturing of the ZnO is lesser than when the copper midlayer is thinner (3 and 4 nm). The pole figure result suggests that although Cu, which typically nucleates with a (111) orientation due to energy considerations, would promote (002) texturing of hexagonal ZnO, in the multilayer structures it does not. This is likely because the copper layers being thin and discontinuous act more as an interference to alignment between the bottom and top ZnO layers than as seed layers for further texturing. This further confirms that the increase in mobility seen at higher Cu thicknesses occurs through metal layer conduction and not due to increased texturing of the ZnO layers.

Fig. 3.10 (a) shows a cross-sectional TEM micrograph from the multilayer structure with a 3 nm copper midlayer. The Cu layer is seen to be in the form of a poorly connected network of islands. This would result in the poor conductivity seen in the multilayer structures with 3 nm Cu midlayer. Fig. 3.10 (b) shows the formation of a contiguous layer at 6 nm of copper layer thickness. This TEM image substantiates the results of electrical and optical characterization, which suggest contiguous layer formation around 6 nm leading to optical transmission and electrical conduction characteristics.

Finally, Fig. 3.10 (c) shows a TEM micrograph from the multilayer structure with an 8 nm copper midlayer. The film is now continuous thus providing an unbroken path for electron conduction as was expected based on Hall conductivity results.

3.5. CONCLUSION

Very high conductivity ZnO/Cu/ZnO films with good transmittance for optoelectronic device applications have been obtained by using the magnetron sputtering technique. For structures with a 6 nm copper layer, the carrier concentration is up to 1.2×10^{22} cm^{-3} and resistivity is 6.92×10^{-5} Ω-cm, values which are an order of magnitude improved compared to existing literature on both multilayer and doped samples. The peak transmittance is still as high as 88%. The film also had a figure of merit of 6.7×10^{-3} Ω^{-1}. Transmission electron microscopy and x-ray photoelectron spectroscopy were used to study the continuity and oxidation state of the copper layer respectively. Finally, very low resistivities with acceptable transmittances have been obtained by depositing a thin copper layer in between two ZnO layers and controlling the thickness such that there is high conductance through the copper layer with minimal loss in transmission due to absorption, reflection, and scattering losses from the copper layer. The films have excellent room temperature conduction and transmission values that compete with those of commercial indium tin oxide. Such results make these ZnO/Cu/ZnO multilayers good candidates for future flexible display applications.

CHAPTER 4

ZnO/Au/ZnO HIGH CONDUCTIVITY TRANSPARENT CONDUCTING OXIDES ON POLYETHYLENE NAPHTHALATE

4. 1. INTRODUCTION

Transparent conducting oxide (TCO) films exhibit high conductivity along with good transparency in the visible region, properties which are usually observed to be mutually exclusive. [1] As a consequence, transparent conductors have generated much recent interest for use in flat-panel displays, solar cells, electrochromic devices, heatable glass, low emittance films for advanced glazing, and protective or decorative coatings. [2-6] The transparent conductor indium tin oxide (ITO) is presently the most used TCO in the optoelectronics industry due to its good electrical conductivity combined with good transmittance (>80%) in the visible spectral range [1]; however, Indium is turning rare and expensive. [7] This makes ITO a non-viable choice for large-scale economical production in the future.

Doped zinc oxide (ZnO) films have been proposed as alternatives to ITO because they have been shown to exhibit comparable properties. [6, 8] Recently, some groups have realized low resistivity ($1\text{-}4\times10^{-4}$ Ω-cm) with good transmittance (about 80%) in the visible range using Ga-doped ZnO films. [6] Indium-doped zinc oxide has also been reported to be an ideal

transparent conducting oxide material for optoelectronic devices, solar cells, and organic LEDs, due to a large work function, a wide transmittance window from 400 to 2500 nm, and a higher chemical etching rate compared to ITO thin films. [9] ZnO also has practical advantages of availability of inexpensive large-area ZnO substrates and good radiation resistance. [10, 11]

The doping approach to improving the properties of transparent conductors is ultimately limited by ionized impurity scattering. Due to this disadvantage, TCOs with sufficiently low resistivity while retaining good optical properties are still unavailable for many applications. [11, 12] An approach involving sandwiching a thin metal layer in a dielectric has been studied in an attempt to increase film conductivity without too much loss in transparency. [13, 14 Silver was first tried as the sandwiched metal layer due to its low resistivity [15,16]. *Han et al.* obtained resistivity as low as 8×10^{-5} Ω-cm but the transparency was only about 75%. Some researchers have also tried copper as the sandwiched metal layer due to its comparable resistivity. [17,18]

Thin gold films are known to exhibit good transmission. [19-21] In this study, the transmittive properties of thin gold films are exploited by sandwiching them in ZnO on flexible polyethylene naphthalate (PEN) substrates to produce very high conductivity and transmittivity films. The electrical, optical and mechanical properties of the films are examined along

with the reasons for the exhibited characteristics.

4.2. EXPERIMENTAL

ZnO thin films have been fabricated using several methods such as magnetron sputtering, spray pyrolysis, chemical vapour deposition, sol-gel technique, pulsed laser deposition, and thermal evaporation. [22-26] Among these techniques, magnetron sputtering is widely used because of the ease of large-area deposition, and advantages such as low deposition temperature, high deposition rate, good adhesion between film and substrate, good surface uniformity, and simple equipment. [27] Hence thin film layers of ZnO and Au were deposited at 10 mTorr pressure by RF magnetron sputter at 100 W and DC sputter at 40 W, respectively onto PEN substrates. The sputtering targets used were 99.999% pure ZnO and 99.99% pure Cu and they were pre-sputtered for 10 minutes prior to deposition to avoid contamination of the films. The base pressure prior to deposition was approximately 1×10^{-7} Torr. The substrate to target distance was 6 cm and maintained constant for all experiments. There was no break in vacuum during deposition of the films. The top and bottom ZnO layers were approximately 30 nm thick while the gold thickness was varied between 1 nm and 12 nm. Bare ZnO layers were deposited under identical conditions for comparison of properties.

Variable angle spectroscopic ellipsometry (VASE) was used for thickness determination of the films. Electrical resistivity, Hall mobility and

carrier concentration were determined by Hall measurements in the van der Pauw geometry using the Ecopia HMS 3000. Four-point-probe analysis was used for sheet resistance measurements.

Optical transmittance and reflectivity were measured using an Ocean Optics double channel spectrometer (model DS200) in the wavelength range 300-900 nm with an aluminum mirror as the reference for reflectivity and a bare PEN substrate for transmittance. Tungsten-halogen and deuterium lamps were used for the visible and UV light sources, respectively.

Transmission electron microscopy (TEM) using a Philips CM200-FEG TEM operating at 200kV was used to confirm the thickness of the Cu midlayer and study the continuity of the metal layer.

Annealing studies were carried out in air for up to 96 hours inside a mechanical furnace at a temperature of 85 ^{o}C.

Static bend testing studies were also carried out on the sample. The sample was bent once, bent and held static for 24 hours at room temperature, and bent and held static for 24 hours at 85 ^{o}C. Optical imaging was done to examine for cracks after bend testing.

A 2.45 GHz, 1300 W single mode cavity applicator microwave system was used for thermal processing of the samples. Temperature profiles on the sample surface were monitored using a Raytek Compact MID series pyrometer.

4.3. RESULTS

Figure 4.1 shows the change in resistivity of the ZnO/Au/ZnO thin films with change in thickness of the gold layer. The as-deposited ZnO films showed a resistivity of 175 Ω-cm for a 60 nm thick film of ZnO. However, bare ZnO films vary considerably in resistivity with preparation technique and conditions. [18, 28] The effective hall resistivity of the films reduces drastically by six orders of magnitude from 175 Ω-cm for the ZnO dielectric layer to 5.2×10^{-5} Ω-cm for the film with a 12 nm gold layer sandwiched in the ZnO film. The effective hall resistivity curve can be approximately broken down into three regions such that there is a region of smooth resistance decrease, (a), followed by a steep reduction in the resistance, (b), and then a curved region, (c), of gradual decrease that asymptotically approaches the bulk resistance. The measurable sheet resistance values of the films are shown in Figure 4.2. The sheet resistance, like the resistivity, drops substantially from ~ 1 MΩ/sq. with only 2 nm of gold to as low as 6.5 Ω/sq. at 12 nm gold thickness. Region (b), with the sharp drop in sheet resistance, and region (c) with a gradual sheet resistance decrease can also be identified in figure 4.2.

The decrease in resistivity can partly be understood by inspection of the changes in carrier concentration and Hall mobility. The change in carrier concentration with thickness of the gold layer is shown in Figure 4.3.

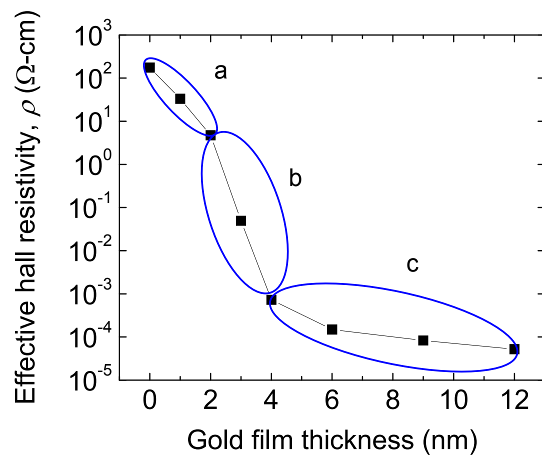

FIG. 4.1. Effective resistivity of the ZnO thin films as a function of embedded gold layer thickness.

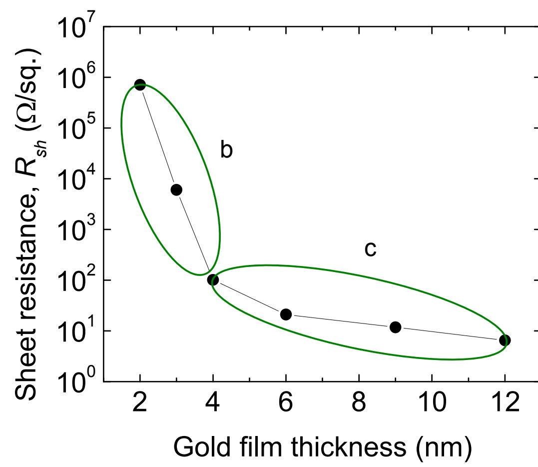

FIG. 4.2. Sheet resistance of the ZnO thin films as a function of embedded gold layer thickness.

Hall measurements fail to show reliable carrier concentration and mobility values at lower gold thickness due to the high resistivity of the samples. However, it can be seen that the variation in carrier concentration with film thickness is almost linear in the range in which the values are measurable. The maximum carrier concentration was up to 1.1×10^{22} cm^{-3}. The variation of Hall mobility with gold film thickness is shown in Figure 4.4. There is a huge jump in mobility from ~ 2 cm^2/V-s at 4 nm gold thickness to 6.8 cm^2/V-s at 6 nm gold thickness. There after there is a more gradual increase in the mobility up to a maximum of ~ 11 cm^2/V-s.

Figure 4.5 shows optical transmission spectra relative to the PEN substrate for the ZnO/Au/ZnO thin films for varying gold layer thickness. The optical transmittance of undoped ZnO films is about 90% over the visible range of wavelengths. Upon insertion of a gold layer the average transmission drops to between 75% and 85% for the ZnO/Au/ZnO structure. However, the variation in transmittance with gold thickness is different in the shorter blue wavelengths compared to the longer red wavelengths. In the wavelengths near the blue part of the visible spectrum, as the thickness of the gold layer increases, the transmission drops. However, in the wavelengths in the red part of the visible spectrum, as the gold layer thickness decreases from 12 nm to 6 nm, the transmission increases but thereafter the transmission drops with reduction in gold thickness.

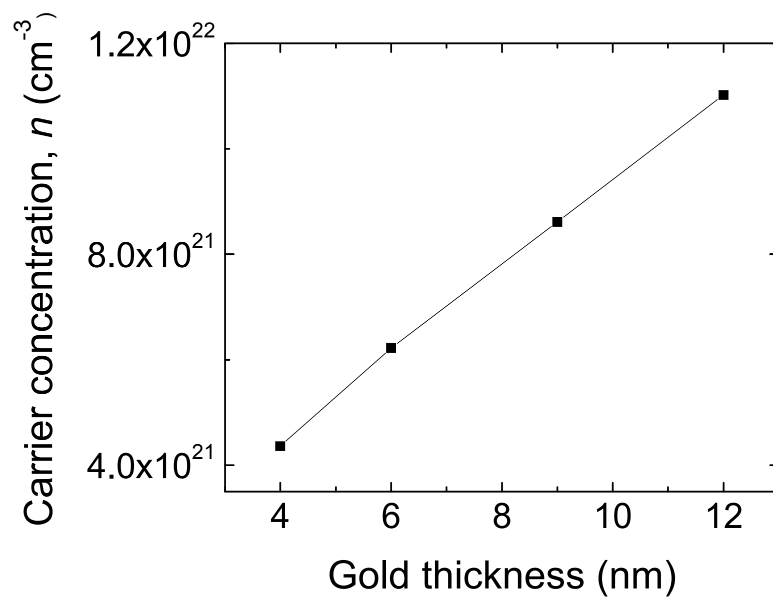

FIG. 4.3 Carrier concentration of the ZnO thins films as a function of embedded gold layer thickness.

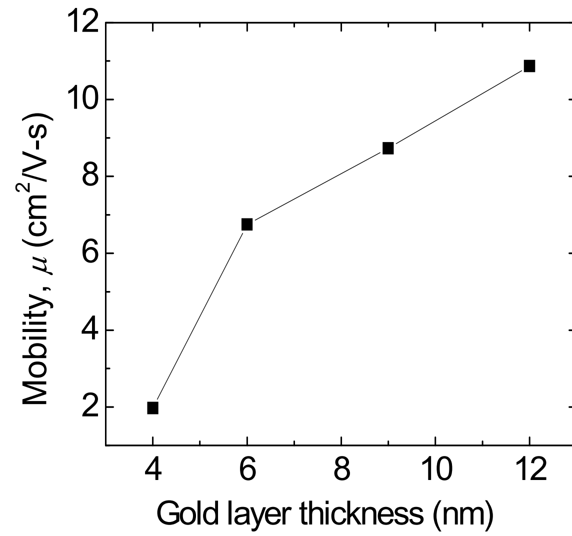

FIG. 4.4. Hall mobility the ZnO thins films as a function of embedded gold layer thickness.

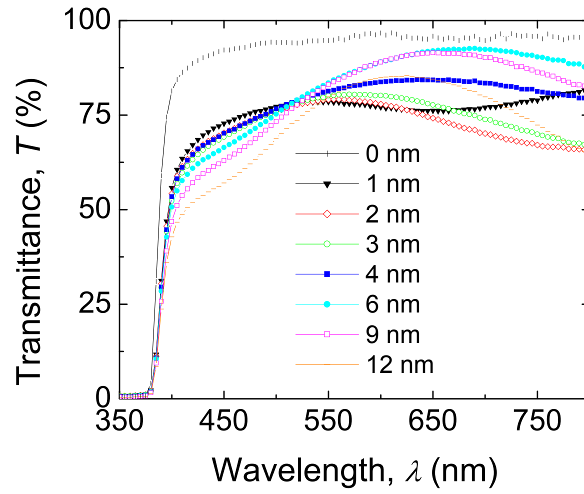

FIG. 4.5. Transmission spectra (relative to the substrate) in the visible spectral range for ZnO thin films showing variation with thickness of the embedded gold layer.

Annealing studies were carried out in air for up to 96 hours inside a mechanical furnace at a temperature of 85 ^{o}C. Sheet resistance in Ω/sq. as a function of annealing time for a thin (3 nm) and thick (12 nm) gold film in the ZnO/Au/ZnO structures is shown in Table 4.1. There was found to be little change in the sheet resistance of the films post-annealing.

Static bend testing studies were also carried out on the films. The films were bent once, bent and held static for 24 hours at room temperature, and bent and held static for 24 hours at 85 ^{o}C. Table 4.2 shows sheet resistance in Ω/sq. under different static bend conditions on a tube of 2" diameter for a thin (3 nm) and thick (12 nm) gold film in the ZnO/Au/ZnO structures. There was found to be no deterioration in the sheet resistance of the samples. Optical microscope images of the film before and after bend testing is shown in Figure 4.6. No new cracks are found to be created from the bend testing experiments.

4.4. DISCUSSION

When very low thickness metal films are sputtered, they tend to be discontinuous and highly resistive. [18, 28] The resistivity of the sputtered ZnO/Au/ZnO films are high initially and decreases gradually with increasing thickness of the gold nanolayer up to 2 nm, as shown in region (a) of Figure 4.1. Accurate estimation of sheet resistance and mobility values from the four-point-probe technique and hall measurement respectively is rendered difficult by the high resistivity of the films. Activated tunneling or thermionic

Table 4.1. Sheet resistance in Ω/sq. as a function of annealing time for a thin (3 nm) and thick (12 nm) Au film in the ZnO/Au/ZnO structures.

Au thickness/Time of anneal	0 hrs	24 hrs	96 hrs
3 nm	6271 ± 418	6280 ± 312	6259 ± 504
12 nm	7.1 ± 0.2	7.1 ± 0.2	7.1 ± 0.2

Table 4.2. Sheet resistance in Ω/sq. under different static bend conditions on a tube of 2” diameter for a thin and thick Au film in the ZnO/Au/ZnO structures.

Bend condition/Au thickness	3 nm	12 nm
as-deposited	7.463929	2.226041
1 second bend	7.723795	2.231238
as-deposited	8.128031	1.929072
24 hrs room temperature bend	7.36287	1.878109
As dep	8.113594	1.765501
24 hrs 85 ^{o}C bend	7.449492	1.652026

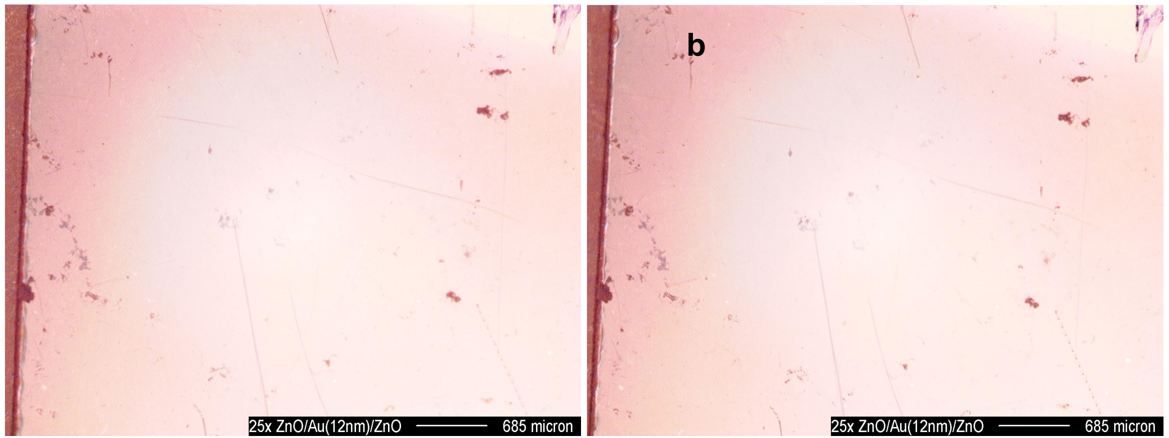

FIG. 4.6. Nomarski images of ZnO/Au(12nm)/ZnO (a) before and (b) after static bend testing.

emission and conduction through the dielectric dominate when the metal islands are small and separation between islands is large. [29, 30] This process is illustrated in the schematic in Figure 4.7. The conductivity in this regime is governed by the equation [31]:

$$\sigma \propto \exp(-2\beta s - \frac{W}{kT}) \qquad (1)$$

where β is the tunneling exponent of electron wavefunctions in the insulator, s is the island separation, W is the island charging energy, k the Boltzmann constant, and T is the temperature. As can be seen from equation (1), the spacing between the islands and the size of the islands, which affects the island charging energy W , play a critical role in determining the overall conductivity. As the islands grow, the gap between the islands reduces and some of the islands undergo large scale coalescence.[32] This leads to a drastic reduction in resistance as observed in region (b) in Figure 1 and also in the sharp drop in sheet resistance values between 2 nm and 4 nm in Figure 4.2. Bulk conduction takes place through the coalesced islands and tunneling occurs between the larger islands with small gaps between them.[33] The mobility can now be detected by Hall measurement and reads about 2 cm^2/V-s. After the large scale coalescence occurs, there is a transition from discontinuous gold islands dispersed in a dielectric matrix to a contiguous film with holes. This is shown as region (c) in Figure 4.1, and can also be identified as the region

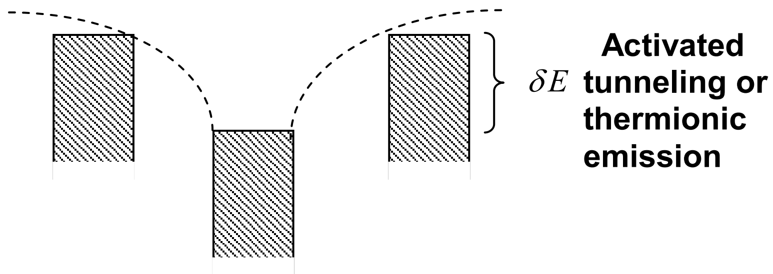

FIG. 4.7. Schematic showing the band diagram for small metal particles with significant separation between them.

between 6 nm and 12 nm gold thickness in Figure 4.2. The formation of this near-continuous film by 6 nm of gold thickness is supported by the jump in mobility to 6.75 $cm^2/V\text{-}s$ as shown in Figure 4.4. This thickness is close to the value at which gold is known to form a continuous film on glass.[34] In the neighborhood of the transition, the curve resembles a hyperbola if the islands and bridges grow at the same rate.[35] The network film becomes a continuous film through the filling of the voids. Nucleation takes place in the voids and the new grains are incorporated in the film.[36] At this stage, the main contribution to the resistance comes from diffuse scattering of the conduction electrons at the Au-ZnO interfaces, grain boundaries, and defects.[37] The mobility in this region can be seen to increase gradually with thickness due to reduction of interface scattering and nominal grain growth. The measured carrier concentration, shown in Figure 3, increases linearly with thickness consequent to the contribution of the valence electrons of gold for conduction.

Figure 4.5 shows optical transmittance spectra relative to the PEN substrate for the ZnO/Au/ZnO thin films for different metal layer thicknesses. The optical transmittance of undoped ZnO films is about 90% over the visible range of wavelengths. [29] Considering the application of the films to display devices, we have chosen to determine the average transmittance by using the equation:

$$T_{av} = \frac{\int V(\lambda)T(\lambda)d\lambda}{\int V(\lambda)d\lambda} \tag{2}$$

where $T(\lambda)$ is the transmittance and $V(\lambda)$ is the photopic luminous efficiency function defining the standard observer for photometry.[38] Upon insertion of the gold layer, the photopic average transmittance of the ZnO multilayer drops to between 75 % and 85% depending upon the thickness of the gold layer. The optical transmittance properties of the films can be understood in terms of changes in the complex dielectric function, $\varepsilon = \varepsilon' + i\varepsilon''$ for gold. The dielectric function of metals can be decomposed into a bound electron term and a free-electron term. In the shorter wavelengths near the blue part of the visible spectrum, as the thickness of the gold layer increases, the transmission decreases. In this region, the transmission is determined by absorption of light due to interband electronic transitions. In particular, due to the excitation of electrons from the *d*-band to the Fermi surface.[39] With increase in thickness of the gold layer, there are more bound electrons available for excitation and hence the greater drop in transmission. In the red wavelengths, gold films are reflective. For the structure with 12 nm gold, the transmittance is low due to high reflectance. As the gold layer thickness decreases from 12 nm to 6 nm, the transmission increases. However below this thickness, the transmittance decreases again because the gold film becomes discontinuous. In discontinuous gold films, there is a size-dependent variation of the dielectric function due to

limitation of the mean free path of the conduction electrons.[40] In particular, the limitation of the mean free path leads to a correction to the imaginary part of the dielectric function ε_2 of the bulk metal $\varepsilon_{2,m}$ by a second term $\varepsilon_{2,s}$ such that [40]:

$$\varepsilon_2(R) = \varepsilon_{2,m} + \varepsilon_{2,s} = \varepsilon_{2,m} + c/R \tag{3}$$

where c is a constant at a particular wavelength and R is the particle radius. As a consequence, below 6 nm, as the radius of the particles decreases, the transmittance loss increases. Also, it is well-known that the plasma absorption band of noble metals typically lies in the visible spectrum.[41-43] However, in our films we fail to see the peak of the plasma absorption band except at 665 nm wavelength in the 1 nm thick Au film. This is likely because the refractive index of the substrate, zinc oxide, is higher than that of glass, on which most of the studies have been done. This red shifts the peak of the plasma absorption band allowing us to obtain high average transmittances in our films.[41] The optical transmittance results substantiate the inference of formation of a continuous conduction layer at 6 nm of Au thickness arrived at based on conduction behavior.

The energy gap E_g of the structure was determined using the relationship:[44]

$$\alpha(h\nu) \propto (h\nu - E_g)^{1/2} \tag{4}$$

where $h\nu$ is the photon energy. ZnO is reported to have an optical band gap

of ~3.2-3.3 eV [45,46] The optical band gap calculated for our films is ~3.21 eV. Although this value is within the range reported for ZnO band gap, it is more advantageous to utilize the combined band gap of the ZnO+PEN structure because PEN is known to have a band gap of ~3.2 eV.[47]

We have estimated the Haacke figure of merit, φ_{TC}, for the films defined as [48]:

$$\varphi_{TC} = \frac{T_{av}^{10}}{R_{sh}} \tag{5}$$

where T_{av} is the average transmittance and R_{sh} is the sheet resistance. The figures of merit of the films are shown in Table 4.3. It can be seen that from an optoelectronic standpoint thin continuous films provide the best figure of merit.

4.5. CONCLUSION

In conclusion, high conductivity ZnO/Au/ZnO films with good transmittance for optoelectronic device applications have been obtained by using the magnetron sputtering technique. The films were found to undergo a seven orders of magnitude drop in effective resistivity from 200 Ω-cm to 5.2×10^{-5} Ω-cm upon increase of the gold layer thickness from 0 nm to 12 nm. The peak transmittance, best photopic averaged transmittance, and Haacke figure of merit are 93%, 85%, and $15.1\times10^{-3}\ \Omega^{-1}$, respectively. The room temperature properties of these films rival those of commercially available ITO which makes it a promising candidate for commercial exploitation in large-area flexible electronics.

Table 4.3. Haacke figure of merit for the multilayer films with different gold thicknesses

Au thickness (nm)	T (%)	T^{10}	R_{sh} (/sq.)	T^{10}/R_{sh} ($^{-1}$)
2	77.8	0.081	710792.7	1.14×10^{-7}
3	79.1	0.096	6049.36	1.59×10^{-5}
4	81.2	0.125	101.44	1.2×10^{3}
6	84	0.175	21.06	8.3×10^{3}
9	83.3	0.161	11.6	13.8×10^{3}
12	79.3	0.098	6.5	15.1×10^{3}

CHAPTER 5

ZnO BASED TRANSPARENT ANODES FOR OLEDs

5.1. INTRODUCTION

Transparent conducting oxides (TCOs), a class of direct wide band gap semiconductors[1], have generated recent interest for use as transparent electrodes in flat-panel displays, solar cells, and organic light-emitting devices (OLEDs).[2-4] Indium tin oxide (ITO) is the most commonly used electrode material in flat-panel displays because of its good electrical conductivity and transparency in the visible region.[5] However, there is an increase in demand for TCOs having lower resistivity while retaining ideal optical properties.[6] Although ITO has good transmission and conduction properties, it is limited in its conductivity by ionized impurity scattering.[7] Typical ITO films have a conductivity about 5×10^{3} $(\Omega\ \mathrm{cm})^{-1}$ which is inadequate for technologies such as flat-panel displays, and other high brightness light-emitting devices.[8]. The limitations posed by the resistivity of ITO cannot be overcome by geometry as increased thickness for lower sheet resistance and enhanced electrical performance necessarily leads to increased absorbance and inferior optical performance.

Attempts have therefore been made to use ITO-based multilayers to lower resistivity of the electrodes.[9] However, there are other drawbacks to ITO such as high cost due to indium scarcity and strong dependence of

performance on deposition conditions.[1] There have been reports of deleterious diffusion of indium and tin into proximate organic charge transporting or emissive layers. [10-13] Other complications for ITO include that the electrical and optical properties depend on dopant concentration, defects, and vacancies.[14] The lifetime and efficiency of OLEDs using ITO can also be strongly dependent on the interface quality [15] and cleaning procedures used prior to deposition of the organic layers[16]. As a consequence, ITO electrodes can require varying degrees of post-deposition processing. Commonly used post-processing includes thermal annealing to achieve lower resistivity [17] and oxygen plasma treatment to improve hole injection efficiency.[18]. There is also a need for a conductor with better transparency across the visible spectrum, especially in the green-blue region [19]. These challenges motivate exploration of transparent conducting materials systems that could be implemented as improvements or alternatives to the ITO standard.

Research on replacements for ITO electrodes include other conducting oxides, carbon nanotubes, graphene, highly conductive polymers, and metallic microgrids combined with conducting polymers. However, few of these electrodes have yielded device performance comparable to those of ITO. [20]

There have been recent reports on the successful growth of high conductivity ZnO/metal/ZnO multilayer structures.[21,22] Importantly, none

of these materials have been investigated as an anode material in a device structure. In this letter, we follow up on previous work [23] to report on the performance of ZnO/Au/ZnO (ZAZ) nanolayers as anodes for OLEDs, by comparing their performance with a commercial ITO anode.

5.2. EXPERIMENTAL

A 9 nm gold nanolayer was selected for comparison to ITO in this report to represent a good balance between optical and electrical performance. The details of the sputter growth technique used for the ZAZ transparent electrodes has been documented previously. [23] A common problem during sputter deposition of ITO is the formation of spikes on the surface that can kill the device [26]. Profilometry scans revealed that the ZAZ multilayers were spike-free. These multilayer electrodes showed a sheet resistance of about 10 Ω/sq. The resistivity was as low as 8.3×10^{-5} Ω-cm with a carrier concentration of 8.6×10^{21} cm^{-3} and a mobility of about 9 cm^2/V-s. The photopic averaged transmittance in the visible spectrum was found to be about 85% while peak transmittance was up to 91.5%. To demonstrate the effect of improved electrical properties of the ZAZ electrodes, OLED devices were fabricated on glass with both the sputter grown ZAZ electrodes and the commercial ITO electrodes. All device layers subsequent to the anode were grown simultaneously. Prior to deposition of the organic layers, the glass substrates and anode materials were cleaned in ultra sonic baths of detergent, DI water, acetone, and isopropanol. Wet

cleaning was followed by a UV/Ozone treatment for 30 minutes in a Jetlight model 4200 cleaner to further remove surface contaminants. Then a 45nm layer of poly(3,4-ethylenedioxythiophene) poly(styrenesulfonate) (PEDOT:PSS) was deposited by spin-coating and thermal processing at 180 ˚C for 50 minutes. The substrates were then loaded into vacuum where 40nm NPD (N,N′-diphenyl-N,N′-bis(1-naphthyl)-1,1′-biphenyl-4,4″-diamine), followed by 40nm Alq_3 (Tris(8-hydroxyquinolinato)aluminium), 1 nm LiF, and 90 nm of Al were thermally deposited. The devices were stored and optically and electrically characterized in a N_2 glovebox. Current-voltage measurements were performed using a Kiethley 2400 source meter and optical power measurements were performed using a Newport 818 calibrated Si photodiode. Electroluminescence (EL) spectra were collected with an Ocean Optics USB2000 spectrometer.

5.3. RESULTS AND DISCUSSION

The current-voltage characteristics are shown in Figure 1. It can be seen from the magnified image of region *a* that in the low voltage regime there is lesser leakage in the devices with ZAZ electrodes than with ITO electrodes. It was found through atomic force microscopy (AFM) analysis that the ZAZ electrodes have a negligible surface roughness. The AFM image shown in Fig. 2 shows a 5 μm x 5 μm scan of the surface morphology of the ZAZ electrode. Analysis using the PicoScan AFM software showed an RMS roughness, and average roughness of the order of 1 nm. At this resolution there is the also the possibility of some system noise interfering

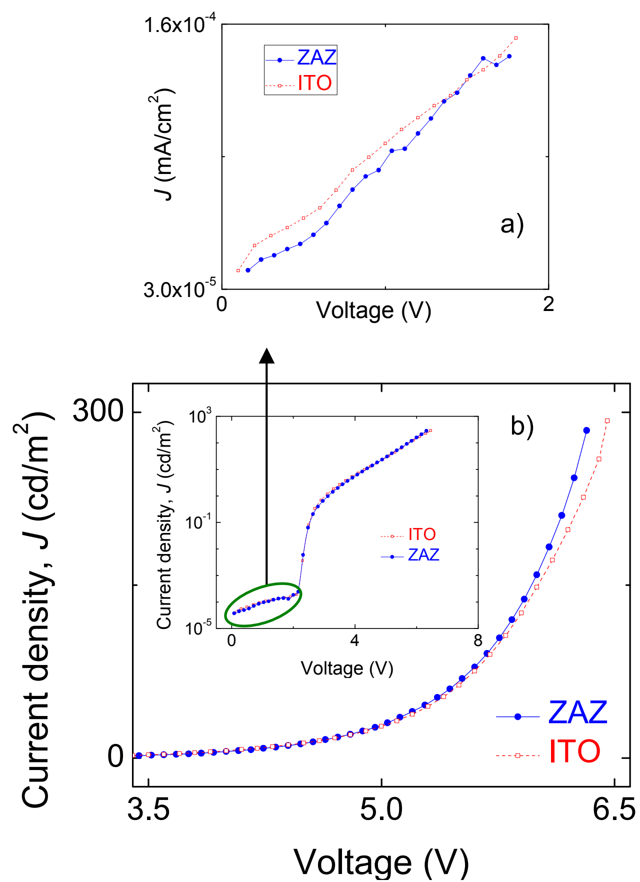

FIG. 5.1. Current density as a function of voltage for OLEDs using ITO and ZAZ multilayers as anodes.

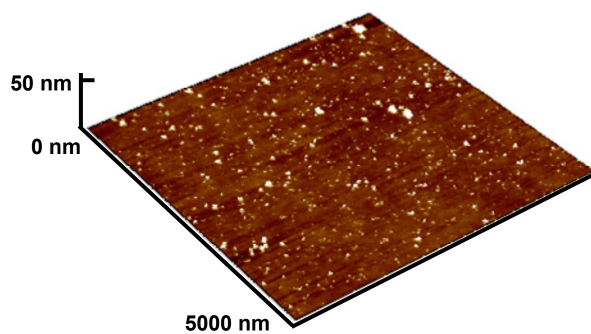

FIG. 5.2. A 5 μm × 5 μm AFM scan showing the surface morphology of the ZAZ anodes

with the signal. Therefore, some of the peaks in the AFM image might be noise. The smoothness of the ZAZ electrodes results in a good interface with the PEDOT layer and smoother interfaces and uniform thicknesses for the organic layers. It is known that the large surface roughness of the ITO substrate induces layer inhomogeneities, especially for the vapor deposited organic layers.[27]. The reduction of this roughness with ZAZ electrodes would imply fewer surface irregularities and interface states. A smooth surface would also reduce inhomogeneous nucleation of evaporated crystallizable layers, *viz*, Alq3. These factors would result in a reduced leakage current prior to device turn-on. After turn-on, it can be seen from region *b* of Fig. 1 that the current-voltage slope is steeper with the ZAZ electrodes than with the ITO electrodes. This difference is seen clearly in the inset Fig. 1. This implies reduced ohmic losses due to the high conductivity of the ZAZ electrodes as there is no difference in the emissive layers. The extent of enhancement in device performance using the ZAZ electrodes can vary slightly depending on the particular geometry and resistance of that anode transmission line.

Figure 3 shows the luminance versus voltage characteristic of the device. The lum/W efficiency of the device improved distinctly at higher voltages in the ZAZ electrodes when compared to the ITO electrodes due to the reduction in ohmic losses. At a luminance of 25000 cd/m^2, the lum/W efficiency of the ZAZ electrode based device improved by about 5%

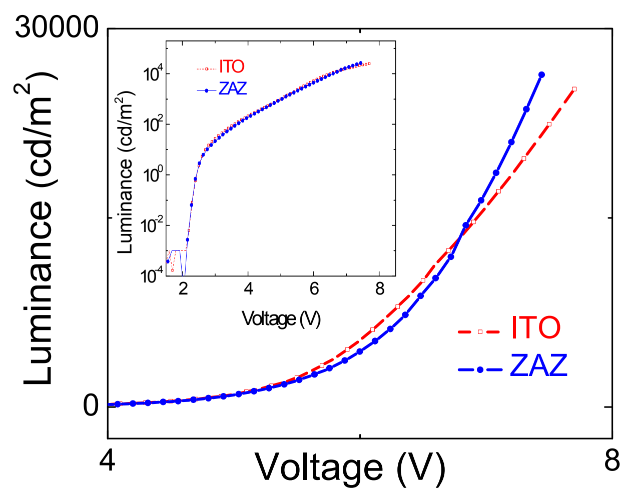

FIG. 5.3. Luminance as a function of voltage for OLEDs using ITO and ZAZ multilayers as anodes.

compared to that of the ITO based device. This reduction in ohmic losses in the anode is especially advantageous for high-brightness and passive-matrix displays where higher momentary brightness is necessary, and ITO transmission lines are long and narrow.[9]

Figure 4 shows the spectral output from the OLEDs with the ZAZ and ITO electrodes. The peak wavelength appears to have red-shifted by 4 nm when using the ZAZ electrodes. The spectral width is also broadened significantly in the green wavelength region, suggesting a more greenish photopic output from the OLED. Thus the ZAZ electrodes allow for a broader spectral output, particularly in the green region, thereby affording great potential for use along with broad-spectrum or green light emitting devices.

5.4. CONCLUSION

Very high conductivity ZAZ electrodes were tested as replacement anodes for ITO anodes. They were found to have reduced leakage and lesser Ohmic losses at high current densities, making them particularly useful for high brightness OLEDs and flat-panel display technology. The presence of the gold layer could also render flexibility to the ZnO/Au/ZnO (ZAZ) electrodes as candidate materials for the development of flexible plastic electronics. The ZAZ electrodes enable better color output in the green spectrum when compared to ITO. Finally, it should be noted that while this letter demonstrates the potential for replacing ITO with ZnO-based anodes, it still understates the anode's performance capacity as the devices

grown were seen to fail sooner than the ITO-based devices due to lateral inhomogeneities in the ZnO layers created during the sputter process in our system. Thus there is scope for process improvement which would result in even better device performance compared to conventional ITO electrodes, making a strong case for ZnO-based multilayer anodes.

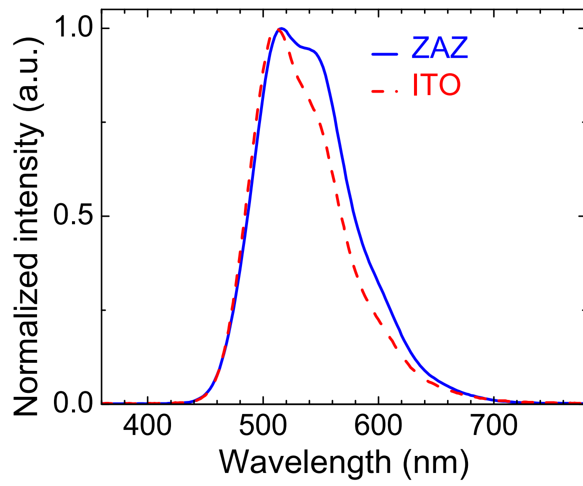

FIG. 5.4. Spectral output from the OLEDs with ITO and ZAZ as electrodes

CHAPTER 6

CONCLUSIONS

6.1. SUMMARY OF RESEARCH

In conclusion, the research done in this body of work has enabled a study of the properties and suitability of ZnO-based thin films with a view to engineering them for optoelectronics applications, making them an effective alternative to indium tin oxide, the most used transparent conducting oxides in the industry.

The first study undertaken to examine the behavior of silver contacts to ZnO and ITO during thermal processing, a step frequently used in materials processing in optoelectronics, revealed that the agglomeration of the silver films at higher temperatures can be delayed considerably by small increases in thicknesses of the deposited metal. Four point probe measurements showed that the silver films showed an abrupt change in resistivity beyond an onset temperature that varied with thickness of the film. Rutherford backscattering spectrometry measurements suggested agglomeration of the Ag films upon annealing. This was then shown to be a causing the resistivity change. X-ray pole figure analysis helped understand that the annealed films took on a preferential (111) texturing; however, the degree of texturing was significantly higher in Ag/ZnO/Si than in Ag/ITO/Si samples. This observation was can be understood by the necessity for

interface energy minimization. Atomic force microscopy revealed an increasing surface roughness of the annealed films with temperature. The resistivity behavior could be understood in terms of the opposing effects of increasing crystallinity and increasing surface roughness upon the resistivity of the films. The agglomeration behavior of the silver films was well-modeled using the Ostwald ripening theory.

The second study, in chapter 3, involved an attempt to improve the conductivity of ZnO films by inserting a thin copper nanolayer between two ZnO layers. This was found to result in higher conductivity than can be obtained by a traditional doping approach. The Hall resistivity of the films was as low as 6.9×10^{-5} Ω-cm with a carrier concentration of 1.2×10^{22} cm^{-3} at the optimum copper layer thickness. The physics of conduction in the films was examined. The conduction involves charge transparent through the metal layers under optimum conditions with minimized scattering losses once the film is just continuous. The transmittances were found to be lower than can be obtained by doping and reasons for transmission losses have been analysed. The peak transmittance of the films was 88% and the photopic averaged transmittance was 75%. Optical transmission behavior of the films was understood to involve absorption by copper due to *d*-band to Fermi-surface transitions at short wavelengths and interface scattering losses at long wavelengths. The Burstein-Moss effect, a shift in the band gap of semiconductors with high extrinsic carrier concentration, was

observed in the films. The effect increased with increase in thickness of the metal nanolayer. The Haacke figure of merit was calculated for all films. The best value obtained was $8.7\times10^{-3}\ \Omega^{-1}$ at optimum metal thickness. Pole figure analysis revealed that the copper midlayer acts as a hindrance to (002) texturing of the top ZnO layer. This has the implication that rather than act as a seed layer, the metal islands hinder preferentially oriented growth of the ZnO films. This would further substantiate the argument that substantial enhancement in conduction is due to the presence of the fine metal network and not due to increase in ZnO crystallinity. The results of the study are important in light of the fact that thermal processing at 150 ^{o}C for up to 24 hours in a reducing (Ar+5% H_2) ambient was found to provide negligible improvement in film properties. This has the implication that on flexible polymer substrates it is critical to have superior as-deposited properties due to the limited scope for thermal annealing related improvement.

In the follow-up study to the copper-based films, described in chapter 4 of this document, the need to improve the average visible transmittance prompted the replacement of copper with gold. Transparent conducting ZnO/Au/ZnO films were grown by the magnetron sputtering technique. The films were found to undergo a seven orders of magnitude drop in effective resistivity from 200 Ω-cm to 5.2×10^{-5} Ω-cm upon increase of the gold layer thickness from 0 nm to 12 nm. The sheet resistance also showed a

substantial decrease to a low 6.5 Ω/sq. The films displayed a photopically average transmittance between 75% and 85% depending upon the gold thickness, and a peak transmittance of up to 93%. The best Haacke figure of merit was $15.1\times10^{-3}\ \Omega^{-1}$. As the gold layer thickness was increased, the conduction changed from conduction through the substrate when the nanometal islands are small and far apart to activated tunneling between discontinuous islands, and finally to direct tunneling between larger islands and metallic conduction through a near-continuous layer. Optical transmission behavior of the films has was understood to comprise gold's absorption due to interband electronic transitions in the shorter visible wavelengths, and free carrier absorption losses at the longer red wavelengths. This was combined with the limitation of the mean free path in discontinuous films in the longer visible wavelengths. In other words, the dielectric constant of the small gold particles exhibits a size dependence that enhances absorption. Low temperature thermal processing of the multilayer ZnO/Au/ZnO films for up to 96 hours at 85 ^{o}C lead to no deterioration in the properties while the films also remained intact when subject to room temperature static bend testing and high temperature static bend testing. Thus the films are shown to be robust to environmental harshness making them a suitable choice for commercial exploitation in large-area flexible electronics.

Finally, chapter 5 takes up on the promise of the films grown in

chapter 4 to test the suitability of the multilayer films for practical application in the optoelectronics industry as a transparent anode for organic light emitting diodes. The electrical and optical characteristics of the organic light emitting diodes with the ZnO-based transparent electrode were compared at every stage with that of an OLED grown on a commercial control ITO electrode. The ZnO/Au/ZnO (ZAZ) multilayer based electrodes exhibited substantially enhanced conductivity (about $8x10^{-5}$ Ω-cm) over conventional indium tin oxide (ITO) electrodes and photopic average transmittance of nearly 85%. OLEDs fabricated with the ZAZ electrodes showed reduced leakage compared to control OLEDs on ITO. Atomic force microscopy revealed ultra-smooth surfaces on the ZnO. This leads to better interfaces between the ZAZ anode and the subsequent organic layers, reducing leakage currents. It was also found that ohmic losses at high current densities were reduced by the usage of the ZAZ electrodes. This is because the higher conductivity of the electrodes will lead to better current transport and lowered losses when the current densities are so high that a lower conductivity electrode like the ITO might suffer from significant losses and consequent overheating. This overheating would have the added effect of being detrimental to the stability of the organic layers. A normalized intensity graph of the colour output from the green OLEDs shows that ZAZ electrodes allow for a broader spectral output in green wavelength region of peak photopic sensitivity compared to ITO. The results documented in this

final chapter serve as a fitting finale to a body of work that started off with characterizing and studying the properties of these new ZnO-based films but culminates in showing their superior properties for used as transparent electrodes in any number of commercial devices including but not limited to organic light emitting diodes, flat panel displays, and photovoltaics.

7.2. FUTURE WORK

It would be interesting to see how this body of work may be carried forward with application not just to organic light emitting diodes, as demonstrated, but also to flat-panel displays and perhaps even photovoltaics. Besides, extension of this research for application to other devices, it would be tremendously useful to tackle the problem of creating *p*-type ZnO films. Not only is this a big challenge in the area of ZnO research, but success if achieved would also enable the creation of homojunction LEDs. Besides, it would open up a whole area of research based on *n*-channel ZnO transistors. Also, it might be useful to understand the properties of multimetal transparent conducting oxides like Zinc Indium Oxide and Indium Gallium Zinc Oxide. The presence of multiple metals with non-directional bonding orbitals could lead to higher mobility thin film transistors than is currently possible using conventional amorphous silicon-based thin film transistors which are limited in mobility.

REFERENCES

CHAPTER 1

1. G.J. Exarhos, X.D. Zhou, Thin Solid Films **515**, 7025 (2007)

2. C.G. Granqvist, A. Hultaker, Thin Solid Films **411,** 1 (2002)

3. Roy G. Gordon, MRS Bulletin **25**, No. 8 (2000)

4. B. Lewis, D. Paine, MRS Bulletin **25**, No. 8 (2000)

5. D. H. Zhang *et al.,* Appl. Phys. A **62**, 487 (1996)

6. K.L. Chopra *et al.,* Thin Solid Films **102**, 1 (1983)

7. D.B. Laks, C.G. Van de Walle, G.F. Neumark, and S.T. Pantelides, Phys. Rev. Lett. **66,** 648 (1991)

8. T. Nakada, Y. Ohkubo, and A. Kunioka, Japan. J. Appl.Phys. **30**, L3344 (1991)

9. N. Izyumskaya *et al.,* phys. Stat. sol. (b) **244**, No. 5 (2007)

10. Lee and Chang, Physical Review B **70,** 115210 (2004)

11. Minami, Semicond. Sci. Technol. **20**, S35 (2005)

12. J. Lewis, S. Grego, B. Chalamal, E. Vick, and D. Temple, Appl. Phys. Lett. **85**, 3450 (2004)

13. S. Fukuda, S. H. N. Lim, and A Anders, Thin Solid Films **516** (2008), 4546

14. R. Lazzari and J. Jupille, Surf. Sci. **482**, 823 (2001)

15. H. K. Park, J. A. Jeong, Y. S. Park, S. I. Na, D. Y. Kim, and H. K. Kim, Electrochemical and Solid-State Letters **12**, H309 (2009)

16. E. Kusano, J. Kawaguchi, and K. Enjouji, J. Vac. Sci. Technol. A **4**, 2907 (1986)

17. N. Jedrecy, G. Renaud, R. Lazzari, and J. Jupille, Phys. Rev. B **72**, 045430 (2005)

18. J. van de Lagemaat, T. M. Barnes, G. Rumbles, S. E. Shaheen, T. J. Coutt, C. Weeks, I. Levitsky, J. Peltola, and P. Glatkowski, Appl. Phys. Lett. **88**, 233503 (2006)

19. V. Bhosle, J. T. Prater, F. Yang, D. Burk, and S. R. Forrest, J. Appl. Phys. **102**, 023501 (2007)

20. J. S. Lewis, and M. S. Weaver, IEEE J. of selected topics in quantum elec. **10**, 45 (2004)

21. C. Lee, R. P. Dwivedi, W. Lee, C. Hong, W. I. Lee, and H. W. Kim, J. Mater. Sci.: Mater. Electron. **19**, 981 (2008)

22. H. C. Kim, T. L. Alford, and D. R. Allee, Appl. Phys. Lett. **22**, 4287 (2002)

23. H. C. Kim and T. L. Alford, J. Appl. Phys. **94**, 5393 (2003)

CHAPTER 2

1. G. J. Exarhos, and X. D. Zhou, Thin Solid Films **515**, 7025 (2007)

2. C. G. Granqvist, and A. Hultaker, Thin Solid Films **411,** 1 (2002)

3. Roy G. Gordon, MRS Bulletin **25**, 52 (2000)

4. B. G. Lewis, and D. C. Paine, MRS Bulletin **25**, 22 (2000)

5. T. Minami, Semicond. Sci. Technol. **20**, S35 (2005)

6. H. Han, D. Adams, J. W. Mayer, and T. L. Alford, J. Appl. Phys. **98**, 083705 (2005)

7. C. G. Van de Walle, Phys. Rev. Lett. **85**, 1012 (2000)

8. N. Izyumskaya, V. Avrutin, U. Ozugar, Y. I. Alivov, and H. Morkoc, Phys. Stat. Sol. (b) **244**, 1439 (2007)

9. X. Fang, T. Ma, M. Akiyama, G. Guan, S. Tsunematsu, and E. Abe, Thin Solid Films, **472**, 242 (2006)

10. A. Anders, E. Byon, D. Kim, K. Fukuda, and S. H. N. Lim, Solid State Comm. **140**, 225 (2006)

11. K. Fukuda, S. H. N. Lim, and A. Anders, Thin Solid Films, **516,** 4546 (2008)

12. L. R. Doolittle, Nucl. Instrum. Methods Phys. Res. B **9**, 344 (1985)

13. Y. Zoo, H. Han, and T. L. Alford, J. Appl. Phys. **102**, 083548 (2007)

14. I. Tomov, M. Adamik, and P. B. Barna, Thin Solid Films **371**, 17 (2000)

15. H. C. Kim, N. D. Theodore, and T. L. Alford, J. Appl. Phys., **95**, 5180 (2004)

16. N. W. Ashcroft, and N. D. Mermin, in *Solid State Physics* (Holt, Rinehart and Winston, USA, 1976)

17. J. R. Greer, and R. A. Street, Acta Materialia **55**, 6345 (2007)

18. H. C. Kim, and T. L. Alford, J. Appl. Phys. **94**, 5393 (2003)

19. D. Soh, Y. Shan, J. Park, Y. Li, and Y. Cho, Physica C **337**, 44 (2000)

20. Y. S. Jung, Appl. Surf. Sci. **221**, 281 (2004)

21. T. J. Klemmer, V. R. Inturi, and J. A. Barnard, J. Vac. Sci. Technol. A **15**, 1190 (1997)

22. N. Fujimara, T. Nishikara, S. Goto, J. Xu, and T. Ito, J. Crystal Growth **130**, 269 (1993)

23. A. E. Lita, and J. E. Sanchez, J. Elec. Matls., **31**, 55 (2002)

24. D. R. Waryoba, and P. N. Kalu, Microsc. Microanal. **11** (Suppl 2), 1694 (2005)

25. M. Birkholz, *Thin Film Analysis by X-Ray Scattering* (Wiley-VCH, Germany, 2006)

26. M. Zinke-Allmang, L. C. Feldman, and S. Nakahara, Appl. Phys. Lett. **51**, 975 (1987)
27. K. Tu, J. W. Mayer, and L. C. Feldman, *Electronic Thin Film Science (*Macmillan, USA, 1992)

28. H. Han, Y. Zoo, J. W. Mayer, and T. L. Alford, J. Appl. Phys. **102**, 036101 (2007)

29. D.J. Srolovitz, and M. G. Goldiner, JOM **47**, 31 (1995)

CHAPTER 3

1. G. J. Exarhos, and X. D. Zhou, Thin Solid Films **515**, 7025 (2007)

2. C. G. Granqvist, and A. Hultaker, Thin Solid Films **411,** 1 (2002)

3. Roy G. Gordon, MRS Bulletin **25**, 52 (2000)

4. B. G. Lewis, and D. C. Paine, MRS Bulletin **25**, 22 (2000)

5. C. Lee, R. P. Dwivedi, W. Lee, C. Hong, W. I. Lee, H. W. Kim, J. Mater. Sci. Electron. **19**, (2008)H. Han, D. Adams, J. W. Mayer, and T. L. Alford, J. Appl. Phys. **98**, 083705 (2005)

6. S. Kim, Y. Moon, D. Moon, M. Hong, Y. Jeon, and J. Park, J. Korean Phys. Soc. **49**, 1256 (2006)

7. D.C. Look, Semicond. Sci. Technol. **20**, S55 (2005)

8. T. Minami, Semicond. Sci. Technol. **20**, S35 (2005)

9. M. Osada, T. Sakemi, T. Yamamoto, Thin Solid Films **494**, 38 (2006)

10. V. Assuncao, E. Fortunato, A. Marques, H. Aguas, I. Ferrira, M.E.V. Costa, R. Martins, Thin Solid Films **427**, 401 (2003)

11. G. Hu, B. Kumar, H. Gong, E.F. Chor, P. Wu, Appl. Phys. Lett. **88**, 101901 (2006)

12. C. G. Van de Walle, Phys. Rev. Lett. **85**, 1012 (2000)

13. N. Izyumskaya, V. Avrutin, U. Ozugar, Y. I. Alivov, and H. Morkoc, Phys. Stat. Sol. (b) **244**, 1439 (2007)

14. C. Guillen, and J. Herrero, Solar Energy Mat. & Solar Cells **92**, 938 (2008)

15. M. Bender, W. Seelig, C. Daube, H. Frankenberger, B. Ocker, and J. Stollenwerk, Thin Solid Films **326**, 72 (1998)

16. D.R. Sahu, S. Lin, and J. Huang, Appl. Surf. Sci. **252**, 7509 (2006)

17. D. R. Sahu, J. Huang, Appl. Surf. Sci. **253**, 827 (2006)

18. D.R. Sahu, and J. Huang, Thin Solid Films **516**, 208 (2007)

19. L. R. Doolittle, Nucl. Instrum. Methods Phys. Res. B **9**, 344 (1985)

20. H. Han, N.D. Theodore, and T.L. Alford, J. Appl. Phys. **103**, 013708 (2008)

21. S. Baik, J. H. Jang, C. H. Lee, W. Y Cho, and K. S. Lim, Appl. Phys. Lett. **70**, 3516 (1997)

22. G. Z. Xing, B. Yao, C. X. Cong, T. Yang, Y. P. Xie, B. H. Li and D. Z. Shen and J. of Alloys and Compounds **457**, 36 (2008)

23. S. Poulston, P. M. Parlett, P. Stone, and M. Bowker, Surf. and Inter. Anal. **24**, 811 (1996)

24. K. Sivaramakrishnan, N. D. Theodore, J. F. Moulder, and T. L. Alford, J. Appl. Phys. **106**, 063510 (2009)

25. K. Sivaramakrishnan, and T. L. Alford, Appl. Phys. Lett. **94**, 052104 (2009)

26. H. Fredriksson, B. Persson, and Y. L. Ystrom, Physica Scripta **3**, 169 (1971)

27. T. Andersson, J. Phys. D: Appl. Phys. **9**, 973 (1976)

28. C. J. Adkins, J. Phys.: Condens. Matter **1**, 1253 (1989)

29. K. L. Chopra, L. C. Bobb, and M. H. Francombe, J. Appl. Phys. **34**, 1699 (1963)

30. D. W. Pashley, M. J. Stowell, M. H. Jacobs, and T. J. Law, Phil. Mag. **10**, 127 (1964)

31. K. L. Chopra, and L. C. Bobb, Acta Metallurgica **12**, 807 (1964)

32. G. Haacke, J. Appl. Phys. **47**, 4086 (1976)

33. W. G. Driscoll, and W. Vaughan, *Handbook of Optics* (McGraw-Hill, USA, 1978)

34. H. Ehrenreich, and H. R. Philipp, Phys. Rev. **128**, 1622 (1962)D. R. Lide, *CRC handbook of chemistry and physics* (CRC Press, Boca Raton, 1996)

35. K Sivaramakrishnan, T. L. Alford, Applied Physics Letters **94**, 052104 (2009)

36. H. Han, J. W. Mayer, and T. L. Alford, J. Appl. Phys. **100**, 083715 (2006)

37. T. Minemoto, T. Negami, S. Nishiwaki, H. Takakura, and Y. Hamakawa, Thin Solid Films **372**, 173 (2000)

38. S. Choopun, R. D. Vispute, W. Yang, R. P. Sharma, and T. Venkatesan, Appl. Phys. Lett. **80**, 1529 (2002)

39. K. J. Kim, and Y. R. Park, Appl. Phys. Lett. **78**, 475 (2001)

40. V. Bhosle, A. Tiwari, and J. Narayan, Appl. Phys. Lett. **88**, 032106 (2006)

CHAPTER 4

1. H. Han, D. Adams, J. W. Mayer, and T. L. Alford, J. Appl. Phys. **98**, 083705 (2005)

2. J. A. Jeong, Y. S. Park, and H. K. Kim, J. Appl. Phys. **107**, 02311 (2010)

3. R. G. Gordon, MRS Bulletin **25**, 52 (2000)

4. K. Sivaramakrishnan, A. T. Ngo, S. Iyer, and T. L. Alford, J. Appl. Phys. **105**, 063525 (2009)

5. M. D. McCluskey, and S. J. Jokela, J. Appl. Phys. **106**, 071101 (2009)

6. L. Wang, D. W. Matson, E. Polikarpov, J. S. Swensen, C. C. Bonham, L. Cosimbescu, J. J. Berry, D. S. Ginley, D. J. Gaspar, and A. B. Padmaperuma, J. Appl. Phys. **107**, 043103 (2010)

7. C. Lee, R. P. Dwivedi, W. Lee, C. Hong, W. I. Lee, H. W. Kim, J. Mater. Sci. Electron. **19**, 981 (2008)

8. D.C. Look, Semicond. Sci. Technol. **20**, S55 (2005)

9. G. Hu, B. Kumar, H. Gong, E.F. Chor, P. Wu, Appl. Phys. Lett. **88**, 101901 (2006)

10. C. G. Van de Walle, Phys. Rev. Lett. **85**, 1012 (2000)

11. N. Izyumskaya, V. Avrutin, u. Ozugar, Y. I. Alivov, and H. Morkoc, Phys. Status Solidi B **244**, 1439 (2007)

12. J. R. Bellingham, W. A. Phillips, and C. J. Adkins, J. Mat. Sci. Lett. **11**, 263 (1992)

13. T. J. Coutts, D. L. Young, and X. Li, MRS Bulletin **25**, 58 (2000)

14. C. Guillen, and J. Herrero, Solar Energy Mat. & Solar cells **92**, 938 (2008)

15. H. Han, N.D. Theodore, and T.L. Alford, J. Appl. Phys. **103**, 013708 (2008)

16. D.R. Sahu, S. Lin, and J. Huang, Appl. Surf. Sci. **252**, 7509 (2006)

17. D. R. Sahu, J. Huang, Appl. Surf. Sci. **253**, 827 (2006)

18. K. Sivaramakrishnan, N. D. Theodore, J. F. Moulder, and T. L. Alford, J. Appl. Phys. **106**, 063510 (2009)

19. T.A. Postlethwaite, J.E. Hutchison, K.W. Hathcock, and R.W. Murray, Langmuir **11**, 4109 (1995)

20. P.A. DiMilla, J.P. Folkers, H.A. Biebuyck, R. Harter, G. P. Lopez, and G. M. Whitesides, J. Am. Chem. Soc. **116**, 2225 (1994)

21. R.A. Hatton, M.R. Willis, M.A. Chesters, and D. Briggs, J. Mater. Chem. **13**, 722 (2003)

22. J. Petersen, C. Brimont, M. Gallart, G. Schmerber, P. Gilliot, C. Ulhaq-Bouillet, J. Rehspringer, S. Colis, C. Becker, A. Slaoui, and A. Dinia, J. Appl. Phys. **107**, 123522 (2010)

23. P. Thakur, V. Bisogni, J. C. Cezar, N. B. Brookes, G. Ghiringhelli, S. Gautam, K. H. Chae, M. Subramanian, R. Jayavel, and K. Asokan, J. Appl. Phys. **107**, 103915 (2010)

24. X. H. Zhang, H. C. Guo, A. M. Yong, J. D. Ye, S. T. Tan, and X. W. Sun, J. Appl. Phys. **107**, 033101 (2010)

25. W. Yan, Q. Jiang, Z. Sun, T. Yao, F. Hu, and S. Wei, J. Appl. Phys. **108**, 013901 (2010)

26. A. Mohanta, and R. K. Thereja, J. Appl. Phys. **104**, 044906 (2008)

27. S. Kim, Y. Moon, D. Moon, M. Hong, Y. Jeon, and J. Park, J. Korean Phys. Soc. **49**, 1256 (2006)

28. G. Z. Xing, B. Yao, C. X. Cong, T. Yang, Y. P. Xie, B. H. Li and D. Z. Shen and J. of Alloys and Compounds **457**, 36 (2008)

29. K. Sivaramakrishnan, and T. L. Alford, Appl. Phys. Lett. **94**, 052104 (2009)

30. R. M. Hill, Proceedings of the Royal Society of London Series A **309**, 377 (1969)

31. C. J. Adkins, J. Phys.: Condens. Matter **1**, 1253 (1989)

32. H. Fredriksson, B. Persson, and Y. L. Ystrom, Physica Scripta **3**, 169 (1971)

33. T. Andersson, J. Phys. D: Appl. Phys. **9**, 973 (1976)

34. T. G. Andersson, and S. H. Norrman, Vacuum **27**, 329 (1977)

35. K. L. Chopra, L. C. Bobb, and M. H. Francombe, J. Appl. Phys. **34**, 1699 (1963)

36. D. W. Pashley, M. J. Stowell, M. H. Jacobs, and T. J. Law, Phil. Mag. **10**, 127 (1964)

37. K. L. Chopra, and L. C. Bobb, Acta Metallurgica **12**, 807 (1964)

38. W. G. Driscoll, and W. Vaughan, *Handbook of Optics* (McGraw-Hill, USA, 1978)

39. V. V. Truong, and G. D. Scott, J. Opt. Soc. Am. **66**, 124 (1976)

40. U. Kreibig, and C. V. Fragstein, Z. Physik **224**, 207 (1969)

41. R. Doremus, Thin Solid Films **326**, 205 (1998)

42. R. H. Doremus, J. Chem. Phys. **40**, 2389 (1964)

43. V. V. Truong, and G. D. Scott, J. Opt. Soc. Am **66**, 124 (1976)

44. H. Han, J. W. Mayer, and T. L. Alford, J. Appl. Phys. **100**, 083715 (2006)

45. T. Minemoto, T. Negami, S. Nishiwaki, H. Takakura, and Y. Hamakawa, Thin Solid Films **372**, 173 (2000)

46. S. Choopun, R. D. Vispute, W. Yang, R. P. Sharma, and T. Venkatesan, Appl. Phys. Lett. **80**, 1529 (2002)

47. H. Han, D. Adams, J. W. Mayer, and T. L. Alford, J. Appl. Phys. **98**, 083705 (2005)

48. Haacke, J. Appl. Phys. **47**, 4086 (1976)

CHAPTER 5

1. D. S. Ghosh, T. L. Chen, and V. Pruneri, *Appl. Phys. Lett.* **96**, 041109 (2010)

2. K. Sivaramakrishnan, A. T. Ngo, S. Iyer, and T. L. Alford, J. Appl. Phys. **105**, 063525 (2009)

3. R. G. Gordon, MRS Bulletin **25**, 52 (2000)

4. D. C. Look, K. D. Leedy, D. H. Tomich, and B. Bayraktaroglu, Appl. Phys. Lett. **96**, 062102 (2010)

5. H. Kim, A. Pique, J. S. Horwitz, H. Mattoussi, H. Murata, Z. H. Kafafi, and D. B. Chrisey, *Appl. Phys. Lett.* **74**, 3444 (1999)

6. S. X. Zhang, S. Dhar, W. Yu, H. Xu, S. B. Ogale, and T. Venkatesan, *Appl. Phys. Lett.* **91**, 112113 (2007)

7. M. A. Morales-Paliza, R. F. Haglund, and L. C. Feldman, *Appl. Phys. Lett.* **80**, 3757 (2002)]

8. J. M. Phillips, R. J. Cava, G. A. Thomas, S. A. Carter, J. Kwo, T. Siegrist, J. J. Krajewski, J. H. Marshall, W. F. Peck Jr., and D. H. Rapkine, *Appl. Phys. Lett.* **67**, 2247 (1995)

9. J. Lewis, S. Grego, B. Chalamala, E. Vick, and D. Temple, *Appl. Phys. Lett.* **85**, 3450 (2004)

10. A. J. Miller, R. A. Hatton, G. Y. Chen, and S. R. P. Silva, *Appl. Phys. Lett.* **90**, 023105 (2007)

11. K. W. Wong, H. L. Yip, Y. Luo, K. Y. Wong, and W. M. Lau, *Appl. Phys. Lett.* **80**, 2788 (2002)

12. S. T. Lee, Z. Q. Gao, and L. S. Hung, *Appl. Phys. Lett.* **75**, 1404 (1999)

13. A. R. Schlatmann, D. Wilms Floet, A. Hilberer, F. Garten, P. J. M. Smulders, T. M. Klapwijk, and G. Hadziioannou, *Appl. Phys. Lett.* **69**, 1764 (1996)

14. D. S. Ghosh, L. Martinez, S. Giurgola, P. Vergani, and V. Pruneri, *Opt. Lett.* **34**, 325 (2009)

15. J. S. Kim, R. H. Friend, and F. Cacialli, *Appl. Phys. Lett.* **74**, 3084 (1999)

16. A. Andersson, N. Johansson, P. Broms, N. Yu, D. Lupo, and W. R. Salaneck, *Adv. Mater.* **10**, 859 (1998)

17. A. Rogozin, N. Shevchenko, M. Vinnichenko, F. Prokert, V. Cantelli, A. Kolitsch, and W. Moller, *Appl. Phys. Lett.* **85**, 212 (2004)

18. C. C. Wu, C. I. Wu, J. C. Sturm, A. Kahn, *Appl. Phys. Lett.* **70**, 1348 (1997)

19. J. M. Phillips, J. Kwo, G. A. Thomas, S. A. Carter, R. J. Cava, S. Y. Hou, J. J. Krajewski, J. H. Marshall, W. F. Peck, D. H. Rapkine, and R. B. van Dover, *Appl. Phys. Lett.* **65**, 115 (1994)

20. B. O'Connor, C. Haughn, K. H. An, K. P. Pipe, and M. Shtein, *Appl. Phys. Lett.* **93**, 223304 (2008)

21. H. Han, N. D. Theodore, and T. L. Alford, *J. Appl. Phys.* **103**, 013708 (2008)

22. K. Sivaramakrishnan, and T. L. Alford, *Appl. Phys. Lett.* **94**, 052104 (2009)

23. K. Sivaramakrishnan, and T. L. Alford, Appl. Phys. Lett. **96**, 201109 (2010)

24. G. Liu, J. B. Kerr, and S. Johnson, *Synth. Met.* **144**, 1 (2004)

25. Ch. Jonda, A. B. R. Mayer, U. Stolz, A. Elschner, A. Karbach, *J. Mater. Sci.* **35**, 5635 (2000)

APPENDIX A

LIST OF PUBLICATIONS

JOURNAL PUBLICATIONS

1. **K. Sivaramakrishnan**, A. T. Ngo, S. Iyer, and T. L. Alford, "Effect of thermal processing on silver thin films of varying thickness deposited on zinc oxide and indium tin oxide", Journal of Applied Physics **105**, 063525 (2009)

2. **K. Sivaramakrishnan**, and T. L. Alford, "Metallic Conductivity and the role of copper in ZnO/Cu/ZnO thin films for flexible electronics", Applied Physics Letters **94**, 052104 (2009)

3. **K. Sivaramakrishnan**, and T. L. Alford, "The role of copper in ZnO/Cu/ZnO thin films for flexible electronics", Journal of Applied Physics **106**, 063510 (2009)

4. **K. Sivaramakrishnan**, and T. L. Alford, "Conduction and transmission analysis in gold nanolayers embedded in zinc oxide for flexible electronics", Applied Physics Letters **96**, 201109 (2010)

5. **K. Sivaramakrishnan**, N. Bakken, J. Li, and T. L.. Alford, "ZnO-based transparent anodes for organic light-emitting devices" *submitted to* Applied Physics Letters 2010

6. **K. Sivaramakrishnan**, S. Elhalawaty, N. D. Theodore, and T. L. Alford, " ZnO/Au/ZnO high conductivity transparent conducting oxides on polyethylene naphthalate", *submitted to* Journal of Applied Physics 2010

7. A. Bowen, J. Li, J. Lewis, **K. Sivaramakrishnan**, T. L. Alford, and S. Iyer, *accepted to* Thin Solid Films 2010 (*in press*)

8. S. Elhalawaty, **K. Sivaramakrishnan**, N. D. Theodore, and T. L. Alford, "The effect of sputtering pressure on electrical, optical, and structural properties of indium tin oxide on glass", Thin Solid Films **518**, 3326 (2010)

PATENTS PENDING

1. **K. Sivaramakrishnan**, and T. L. Alford, "ZINC OXIDE METAL MULTILAYER STRUCTURE AND METHOD OF PROVIDING SAME", United States Patent

CONFERENCE PRESENTATIONS AND PROCEEDINGS

1. **K. Sivaramakrishnan**, N. D. Theodore, J. F. Moulder, and T. L. Alford, “Metallic Conduction in ZnO/Cu/ZnO Thin Films” , Advanced Metallization Conference 2009 and Materials Research Society Proceedings 2010

2. **K. Sivaramakrishnan**, S. Iyer, N. D. Theodore, and T. L. Alford, “Effect of thermal processing on silver contacts for zinc oxide and indium tin oxide”, Advanced Metallization Conference 2009 and Materials Research Society Proceedings 2010

3. **K. Sivaramakrishnan**, H. Han, N. D. Theodore, S. Iyer, and T. L. Alford, “Embedded silver layer induced conductivity enhancement of zinc oxide on flexible substrates for optoelectronics”, Flexible Electronics and Displays Conference 2009

4. **K. Sivaramakrishnan**, A. Indluru, and T. L. Alford, “Low Temperature Dopant Activation Using Variable Frequency Microwave Annealing”, Materials Research Society Proceedings 2010